Nano Fiber
https://www.sciltp.com/journals/nf

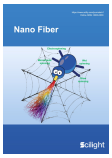

Review

MXene-Based Fibers for Fiber-Shaped Supercapacitors: Fabrication, Structural Engineering, and Wearable Applications

Xiaolin Zhu, Changsong Li and Guan Wu *

State Key Laboratory of Bio-Based Fiber Materials, Zhejiang Sci-Tech University, Hangzhou 310018, China
* Correspondence: gwu2016@zstu.edu.cn; Tel.: +86-158-5294-8803

How To Cite: Zhu, X.; Li, C.; Wu, G. MXene-Based Fibers for Fiber-Shaped Supercapacitors: Fabrication, Structural Engineering, and Wearable Applications. *Nano Fiber* **2026**, *1*(1), 2.

Received: 27 September 2026
Revised: 20 October 2026
Accepted: 6 November 2026
Published: 20 November 2026

Abstract: The rapid advancement of wearable and flexible electronics has created an urgent requirement for fiber-shaped energy storage systems that simultaneously deliver high power and energy densities, outstanding mechanical flexibility, and wearability. Fiber-based supercapacitors (FSCs) are regarded as attractive candidates for energy storage owing to their high-power density, rapid charge/discharge capability, long cycle life, and outstanding mechanical flexibility. MXenes, a family of two-dimensional transition metal carbides/nitrides, have emerged as ideal building blocks for high-performance fiber electrodes because of their metallic conductivity, tunable surface terminations, high volumetric capacitance, and good solution processability. This review summarizes recent advances in MXene-based FSCs, covering MXene synthesis methods such as HF etching, *in situ* HF etching, electrochemical etching, alkali etching, molten salt etching, and halogen etching. It then highlights fiber fabrication strategies including coating, electrospinning, biscrolling, and wet-spinning, with emphasis on the structural regulation and performance optimization of pure MXene fibers, MXene composite fibers, and coaxial fibers. The effects of electrode materials, electrolytes, specific surface area, and pore-size matching on capacitive performance are also discussed. Finally, the wearable applications of MXene-based FSCs in smart textiles and self-powered systems are presented, and remaining challenges such as oxidation stability, interlayer assembly, surface utilization, and scalable manufacturing are outlined. Future efforts should focus on advanced spinning and microfluidic assembly technologies to realize high-performance, stable, and scalable MXene fiber energy storage devices.

Keywords: MXene fiber; supercapacitor; wet-spinning; wearable application

1. Introduction

The continued expansion of wearable and mechanically compliant electronics has intensified the need for flexible energy-storage and power-supply systems capable of delivering high energy and power densities while maintaining excellent deformability and compatibility with wearable applications [1–3]. Among the various flexible energy-storage technologies, flexible fiber-based supercapacitors (FSCs) have attracted considerable attention because they can deliver high power densities of up to 10 kW kg^{-1}, enable rapid charging and discharging, retain stable performance over more than 100,000 cycles, and withstand substantial mechanical deformation [4–6]. In particular, flexible energy-storage devices should maintain their electrochemical performance under mechanical deformation. A broad range of electroactive materials has been explored for fabricating fiber electrodes intended for wearable and smart electronic applications [7,8]. Representative candidates include carbonaceous materials,

Copyright: © 2026 by the authors. This is an open access article under the terms and conditions of the Creative Commons Attribution (CC BY) license (https://creativecommons.org/licenses/by/4.0/).
Publisher's Note: Scilight stays neutral with regard to jurisdictional claims in published maps and institutional affiliations.

such as activated carbon [9,10], carbon nanotubes (CNTs) [11,12], and graphene [13,14], as well as transition-metal oxides (e.g., MnO_2 and RuO_2) [15,16] and conducting polymers [17,18]. Among them, carbon-based electrodes have been extensively investigated because of their large accessible surface area, favorable chemical stability, and relatively low production cost [19,20]. However, conventional carbon materials often suffer from limited charge-storage capacity and relatively low energy density, which restrict their ability to meet the increasing energy requirements of advanced wearable devices. Transition metal oxides and conducting polymers present pseudocapacitive properties thus providing higher specific capacitance, however, the low conductivity of these materials limits their rate performance and practical applications [21,22]. Hence, one of the crucial challenges in the development of flexible and wearable energy storage devices is the fabrication of electrodes with fine flexibility, high conductivity, good mechanical and electrical properties and superior electrochemical stability.

Recently, a promising family of two-dimensional (2D) transition metal carbides and nitrides, collectively known as MXenes, has caused a research boom due to their highly reversible surface redox reactions, exceptional metallic conductivity and notable electrochemical properties [23,24]. MXenes can be generally represented by the formula $M_{n+1}X_nT_x$ (n = 1–3). In this expression, M denotes an early transition metal (e.g., Ti, Zr, V, or Mo), X stands for C, N, or a combination of the two, and T_x denotes the terminal groups on the surface, including -OH, -O, -Cl, and -F [25,26]. Since MXenes were first discovered in 2011, over 30 distinct stoichiometric MXenes have been successfully synthesized, and numerous unique structures and properties have been predicted by theoretical calculations [27]. Among the MXenes that have been synthesized, $Ti_3C_2T_x$ is the most intensively studied and shows promising applications in FSC electrodes [28]. Besides having an ultra-high conductivity, reaching 20,000 S cm^{-1} as thin film, it also has an ultrahigh volumetric specific capacitance (~1500 F cm^{-3}), mainly from H^+ insertion/deinsertion and surface redox reactions [29]. Remarkably, $Ti_3C_2T_x$ MXene has hydrophilic surface due to the presence of T_x functional groups, contributing to good colloidal stability [30]. Growing understanding of the rheological behavior and dispersion of MXenes in various solvents has driven the development of diverse processing methods. These methods enable MXenes to be shaped into new structures and geometries, making MXene an ideal material for functional fibers [31]. Research on MXene fibers originated from efforts to achieve the macroscopic assembly of two-dimensional MXene nanosheets and has progressively evolved from composite-assisted fiber formation and direct spinning of pure MXene fibers to nanosheet orientation, interfacial engineering, hierarchical structural design, and multifunctional device integration, as illustrated in Figure 1. This evolution reflects a gradual shift in the central challenge of MXene fiber research from simply achieving continuous fiber formation toward simultaneously regulating mechanical robustness, electrical conductivity, ion accessibility, environmental stability, and functional adaptability.

In 2017, Seyedin et al. [32] were the first to utilize the excellent fibrillation property of liquid crystalline graphene oxide (GO) to assist in the wet spinning of MXene nanosheets, resulting in the fabrication of woven fibers with a MXene content of approximately 88 wt%. These fibers possess both certain mechanical flexibility and energy storage capabilities, providing an important idea for the assembly of two-dimensional MXene from sheet materials into one-dimensional macroscopic fibers. This also laid the foundation for the application of MXene fibers in fiber energy storage devices and intelligent textiles. Subsequently, the researchers began to explore alternative methods for fabricating fibers beyond wet spinning. In 2018, MXene/carbon nanotube (CNT) fibers were subsequently fabricated through a biscrolling strategy, in which MXene nanosheets were incorporated into CNT sheets followed by twisting and scrolling [33]. The CNT framework provided mechanical support while suppressing excessive MXene restacking, enabling high MXene loading and improved flexibility and electrochemical performance. In 2019, MXene fibers began to be further developed by using carbon materials such as GO and CNT as auxiliary fibers [34]. They were also expanded to include conductive polymers and other functional components as auxiliary fibers. For instance, by combining $Ti_3C_2T_x$ MXene with PEDOT:PSS for wet spinning, continuous conductive fibers with an MXene content of approximately 70 wt% could be obtained, and their electrical conductivity reached 1489.8 S cm^{-1} [35]. The year 2020 represented a major turning point in MXene fiber research with the realization of additive-free pure MXene fibers. Concentrated $Ti_3C_2T_x$ dispersions were found to form liquid-crystalline phases, allowing MXene nanosheets to undergo shear-induced alignment during wet spinning [36]. The resulting pure MXene fibers exhibited electrical conductivity as high as approximately 7748 S cm^{-1}, demonstrating that continuous macroscopic fibers could be directly assembled without GO or polymeric spinning additives. During the same period, scalable additive- and binder-free wet spinning was also developed for meter-scale pure MXene fibers with electrical conductivity reaching approximately 7713 S cm^{-1}, establishing liquid-crystalline wet spinning as a key route toward continuous MXene fiber production. After the successful formation of pure MXene fibers, attention shifted from spinnability to nanosheet alignment and internal structural regulation. In 2021, highly oriented $Ti_3C_2T_x$ fibers were fabricated by controlling spinneret geometry, spinning conditions, and flow-induced alignment, together with Mg^{2+} crosslinking between adjacent MXene

nanosheets [37]. Notably, the obtained fibers combined excellent electrical transport with robust mechanical and electrochemical properties, delivering a conductivity of approximately 7200 S cm^{-1}, a tensile strength of 118 MPa, and a volumetric capacitance of 1360 F cm^{-3}. These results demonstrated that MXene fiber performance is strongly governed not only by MXene content but also by nanosheet orientation, interlayer interactions, and structural defects. Around 2022, increasing attention was devoted to core-shell structures and interfacial reinforcement. High-strength components such as aramid nanofibers (ANFs) were incorporated into MXene fibers, and ANF@MXene core-shell fibers were fabricated through coaxial wet spinning [38]. Interfacial interactions, particularly hydrogen bonding, enhanced the mechanical properties and environmental stability while maintaining the conductive MXene network. This development shifted MXene fiber design from simple orientation control toward the synergistic regulation of alignment and interfacial interactions. Since 2023, increasing emphasis has been placed on mechanical reinforcement, interfacial engineering, and structural optimization of MXene-based fibers. For example, Wang et al. [39] fabricated MXene/cellulose methyl ether (CMC) composite fibers with a pearl-like nacre structure by regulating the interfacial interactions and interlayer spacings between the MXene nanosheets. This study demonstrated the effectiveness of biomimetic structure design in enhancing the mechanical and electrochemical properties of MXene-based fibers, providing a promising strategy for the development of high-performance fibrous energy storage devices. The resulting fibers combined favorable mechanical strength and electrical conductivity, reaching 145.2 MPa and 479.2 S cm^{-1}, respectively, and were further processed into nonwoven mats with potential for electromagnetic interference (EMI) shielding applications. This work demonstrated the transition of MXene fibers from laboratory-scale single-fiber fabrication toward continuous processing and textile integration. By 2024, interfacial engineering and multiscale structural design had become important strategies for further improving MXene fibers [40]. Cellulose nanofibers (CNFs) were introduced to regulate MXene interlayer interactions through hydrogen bonding and electrostatic interactions, thereby improving the rheological behavior of spinning dispersions, fiber mechanical strength, and interlayer spacing. The resulting CNF/MXene fibers exhibited an electrical conductivity of 916 S cm^{-1} and a volumetric capacitance of 1457 F cm^{-3} [41]. Research at this stage increasingly focused on the precise regulation of nanosheet alignment, interfacial bonding, pore structure, ion transport, and stress transfer. Since 2025, the research on MXene fibers has further developed towards intelligence, wearable technology, and adaptability to complex environments [42]. The research focus has gradually shifted from improving the electrical and mechanical properties of individual fibers to the integration of multifunctional capabilities such as woven fibers, flexible sensing, human physiological signal monitoring, thermal management, energy storage and conversion. For instance, recently, MXene/alginate organic hydrogel fibers have been able to be directly woven into fabrics and used for monitoring human movement as well as physiological signals such as electrocardiographic (ECG) and electromyographic (EMG) signals [43].

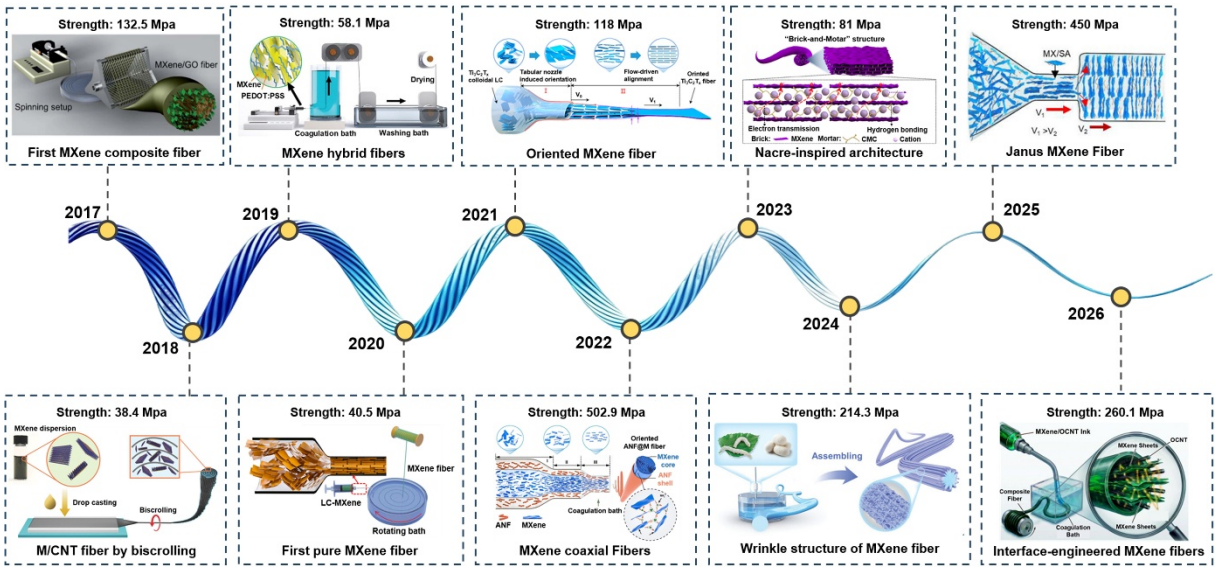

Figure 1. The evolution of MXene-based fibers. (First MXene composite fiber, Reprinted with permission from Ref. [32]. Copyright 2017, Royal Society of Chemistry; MXene/CNT fiber by biscrolling, Reprinted with permission from Ref. [33]. Copyright 2018, Wiley-VCH; MXene/PEDOT:PSS hybrid fibers, Reprinted with permission from Ref. [35]. Copyright 2019, Wiley-VCH; First pure MXene fiber, Reprinted with permission from Ref. [36]. Copyright 2020, American Chemical Society; Oriented MXene fiber, Reprinted with permission from Ref. [37]. Copyright 2021, American Chemical Society; MXene coaxial fibers, Reprinted with permission from Ref. [38]. Copyright 2022,

Springer Nature; Nacre-inspired architecture, Reprinted with permission from Ref. [39]. Copyright 2023, American Chemical Society; Wrinkle structure of MXene fiber, Reprinted with permission from Ref. [40]. Copyright 2024, Wiley-VCH; Janus MXene fiber, Reprinted with permission from Ref. [42]. Copyright 2025, Wiley-VCH; Interface-engineered MXene fibers, Reprinted with permission from Ref. [43]. Copyright 2026, Elsevier.

Despite the considerable progress achieved in MXene-based fiber-shaped supercapacitors (FSCs), several challenges remain before their practical implementation in wearable electronics. In particular, the simultaneous realization of high electrochemical performance, mechanical robustness, long-term environmental stability, and scalable manufacturing remains challenging. The intrinsic tendency of MXene nanosheets toward restacking and oxidation can reduce the accessible electrochemically active surface area and deteriorate electrical conductivity, while the trade-off between mechanical flexibility and energy-storage capability further complicates the structural design of fiber electrodes [44,45]. Moreover, rational control over nanosheet assembly, interfacial interactions, pore structures, and ion-transport pathways is still required to fully exploit the advantages of MXenes in fiber-based energy-storage systems [46,47]. In this review, we first summarize the key factors governing the electrochemical performance of FSCs and discuss representative strategies for MXene synthesis. We then systematically review the fabrication of MXene-based fabrics, yarns, and fibers, including coating, electrospinning, biscrolling, and wet-spinning, with particular emphasis on the structural engineering of pure MXene fibers, MXene-based composite fibers, and coaxial fibers. The relationships between fiber structure, mechanical properties, electrical conductivity, and electrochemical performance are critically discussed. Subsequently, recent advances in MXene-based FSCs for wearable electronics, smart textiles, and self-powered systems are highlighted. Finally, the remaining challenges and future opportunities in MXene fiber assembly, structural optimization, oxidation resistance, and scalable manufacturing are discussed, with the aim of providing guidance for the development of high-performance and practically applicable MXene-based fiber energy-storage devices.

2. Electrochemical Behavior of MXene-Based SCs

The electrochemical performance of MXene-based supercapacitors is intrinsically linked to their unique electronic structure, surface chemistry, and layered architecture. Among the MXene family, $Ti_3C_2T_x$ has emerged as a prominent electrode material owing to its high electrical conductivity, hydrophilic surface, and abundant electrochemically active sites [48]. The metallic Ti-C framework ensures rapid electron transport, while surface terminal groups (T_x, predominantly -O, -OH, and -F) govern electrolyte wettability, interfacial ion dynamics, and redox activity. Concurrently, the two-dimensional layered structure provides accessible interlayer galleries for ion adsorption and intercalation [29]. This unique structural synergy enables $Ti_3C_2T_x$ to exhibit both electric double-layer capacitance (EDLC) and pseudocapacitive energy storage behaviors, with their relative contributions dictated by the electrolyte environment, surface chemistry, and operational potential window [49,50]. Therefore, a comprehensive understanding of these underlying energy storage mechanisms is imperative.

EDLC originates from the electrostatic accumulation of electrolyte ions at the electrode electrolyte interface and does not involve Faradaic electron-transfer reactions [51,52]. For MXene electrodes, this static charge storage occurs not only on the external nanosheet surfaces but also within the interlayer regions accessible to the electrolyte, as depicted in Figure 2a. However, the distribution and transport behavior of electrolyte ions are significantly influenced by their physicochemical properties. Qian et al. [53] systematically studied the electrochemical behavior of $Ti_3C_2T_x$ thin films prepared in free stereochemistry in LiCl, NaCl, and KCl electrolytes in aqueous solutions. As illustrated in Figure 2a, K^+ ions with smaller hydrated radii predominantly undergo surface-related adsorption, whereas Li^+ ions (despite a smaller bare ionic radius but a larger hydration shell) are more prone to partially dehydrate and penetrate the interlayer channels. Consequently, the interlayer spacing in the LiCl system expands more than in the KCl system (1.344 nm vs. 1.305 nm), reflecting the distinct cation occupancy. The CV profiles in Figure 2b further corroborate that electrolyte cations significantly modulate the capacitance response. These observations demonstrate that ion size, hydration behavior, and interlayer accessibility collectively dictate the charge storage process. Notably, electrostatic adsorption and ion intercalation should not be regarded as mutually exclusive; importantly, mere ion intercalation does not necessarily imply Faradaic charge transfer.

Beyond electrostatic storage, MXene exhibits rapid pseudocapacitive behavior via reversible Faradaic reactions at electrochemically active surface sites [54,55]. This contribution is particularly pronounced in acidic electrolytes (e.g., H_2SO_4), where small protons readily penetrate the MXene interlayers and interact with oxygen-containing terminations [56]. During cathodic polarization, the insertion of protons and their interaction with surface oxygen groups are accompanied by electron transfer, promoting the conversion of -O to -OH groups and

altering the oxidation state of Ti. The reverse process occurs during anodic polarization, enabling reversible pseudocapacitive storage, which can be simplified as [57,58]:

$$Ti_3C_2O_x + \delta e^- + \delta H^+ = Ti_3C_2O_{x-\delta}(OH)_\delta \quad (1)$$

As shown in Figure 2c, the reversible protonation and deprotonation of surface oxygen atoms will be accompanied by changes in the electronic state of Ti, thereby achieving pseudocapacitive charge storage [59]. Zhang et al. [59] used *in situ* UV Vis spectroscopy to investigate the electrochemical behavior of $Ti_3C_2T_x$ in different aqueous electrolytes. Their results indicate that the charge storage process related to oxidation-reduction in H_2SO_4 is different from the behavior mainly manifested as electrostatic charging in Li_2SO_4. These findings indicate that the electrochemical activity of MXene is not only determined by its conductive framework, but also influenced by the interactions between electrolyte ions and surface functional groups [60]. In addition, different electrochemical responses indicate that the shape of the cyclic voltammetry curve alone may not be sufficient to identify the charge storage mechanism, especially when ion insertion and interface charging occur simultaneously [61].

In non-aqueous systems, the pseudocapacitive behavior of MXene is additionally complicated by ion solvation/desolvation dynamics [62]. Wang et al. [63] evaluated porous Ti_3C_2 electrodes in lithium bis(trifluoromethylsulfonyl)amine (LiTFSI) electrolytes dissolved in dimethyl sulfoxide (DMSO), acetonitrile (ACN), and propylene carbonate (PC). As depicted in Figure 2d, despite utilizing the same lithium salt, the electrochemical responses vary drastically, with the PC-based electrolyte delivering a significantly higher capacity. This discrepancy is closely tied to the solvation structure of Li^+ during intercalation. In PC-based electrolytes, Li^+ ions undergo extensive desolvation prior to entering the Ti_3C_2 interlayers, whereas in DMSO and ACN systems, pronounced solvent co-intercalation occurs, as illustrated in Figure 2e. Consequently, distinct ion-solvent interactions dramatically alter the interlayer microenvironment and the overall electrochemical response. These results underscore that electrolyte engineering must prioritize the compatibility between solvated ions and the MXene interlayer structure, rather than solely focusing on bulk ionic conductivity [64]. Overall, the electrochemical energy storage behavior of $Ti_3C_2T_x$ MXene is a complex interplay of its electronic conductivity, surface functional groups, layered architecture, and electrolyte-dependent ion dynamics. High electronic conductivity ensures rapid charge transfer, oxygen-containing terminations enable reversible redox reactions, the interlayer structure dictates electrolyte accommodation, and ion solvation characteristics govern the accessibility and kinetics of charge storage [65]. Therefore, enhancing the electrochemical performance of MXene electrodes necessitates a coordinated multi-scale regulation of electron transport, surface chemistry, and ion accessibility, rather than the optimization of a single material parameter.

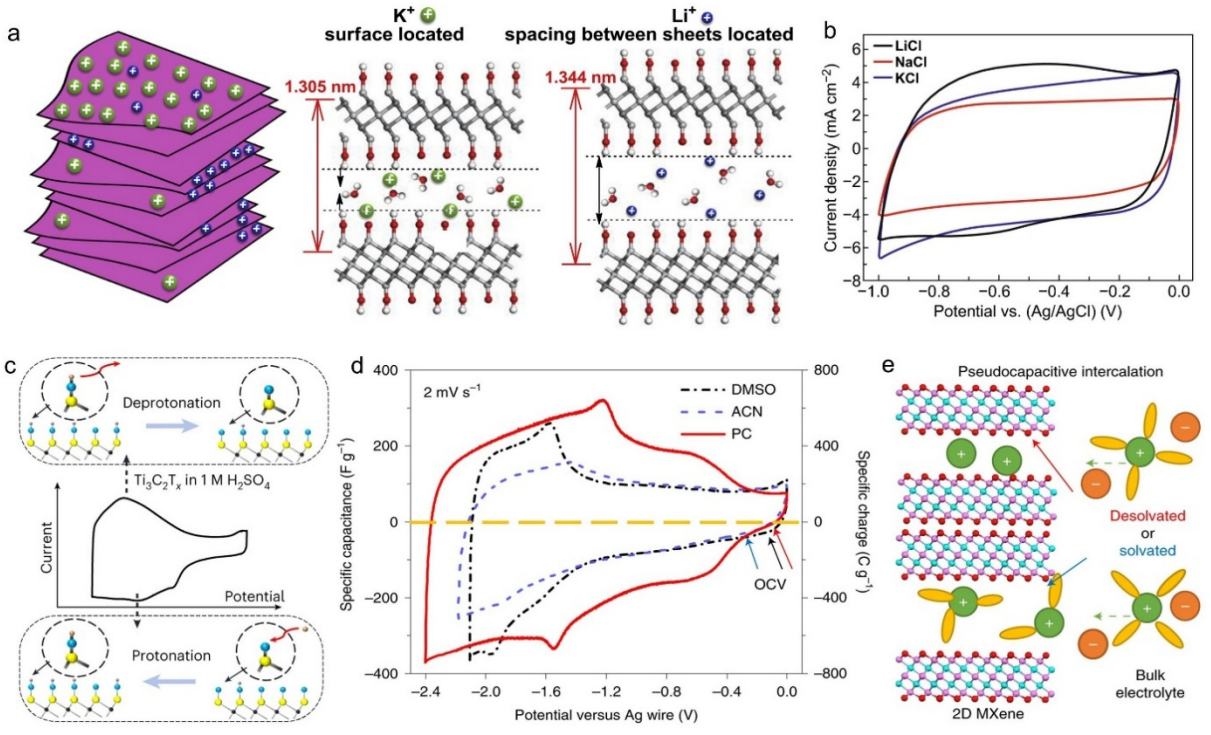

Figure 2. Schematic diagram and representative electrochemical response of $Ti_3C_2T_x$ MXene electrodes in different electrolyte systems. (**a**) Schematic diagram of electrolyte ion adsorption on accessible MXene surfaces and distribution in interlayer regions; (**b**) The CV curves of $Ti_3C_2T_x$ MXene electrode in LiCl, NaCl, and KCl

electrolytes. Reprinted with permission from Ref. [53]. Copyright 2018, Elsevier. (**c**) Schematic diagram of proton coupled pseudocapacitive energy storage where surface oxygen functional groups undergo reversible protonation and deprotonation in H_2SO_4 electrolyte. Reprinted with permission from Ref. [59]. Copyright 2023, Springer Nature. (**d**) The CV curves of porous Ti_3C_2 MXene electrode in LiTFSI organic electrolyte containing DMSO, ACN, and PC solvents. (**e**) Schematic diagram of solvent dependent pseudocapacitive embedding, highlighting the effects of solvation and desolvation of lithium ions on interlayer charge storage. Reprinted with permission from Ref. [63]. Copyright 2019, Springer Nature.

Beyond the intrinsic material and electrolyte properties, the temperature is another factor affecting the electrochemical performance and stability of MXene-based supercapacitors [66]. During repeated charge/discharge cycles, heat is inevitably generated due to internal resistance and electrochemical polarization [67]. While a moderate temperature increase can enhance electrolyte ionic conductivity and accelerate ion transport kinetics (benefiting rate performance), prolonged exposure to elevated temperatures accelerates the oxidation of $Ti_3C_2T_x$, especially in the presence of oxygen and moisture. The formation of insulating titanium oxides disrupts conductive pathways and reduces accessible active sites, leading to a gradual deterioration in capacitance and cycling stability [68,69]. Additionally, elevated temperatures may induce dehydration of hydrogel electrolytes, resulting in reduced ionic conductivity and increased interfacial resistance [70]. Therefore, improved charge transport at moderately elevated temperatures does not necessarily guarantee better long-term device stability. To address this, rational electrode and electrolyte design can extend the operating temperature range. For example, Liu et al. [71] developed an all-solid-state FSC using $Ti_3C_2T_x$/ANFs electrodes and a montmorillonite/polyvinyl alcohol organic hydrogel electrolyte, which maintained favorable electrochemical performance over a wide temperature range from −40 to 80 °C. This demonstrates that the temperature tolerance of MXene-based FSCs depends on the synergistic stability of the MXene electrode, the electrolyte, and the electrode–electrolyte interface. Despite these advances, long-term cycling stability under elevated temperatures remains a critical challenge for practical applications.

3. Synthesis of MXene

MXenes, a family of two-dimensional transition metal carbides and/or nitrides, have attracted considerable attention owing to their unique electronic and electrochemical properties [72]. Their general formula is $M_{n+1}X_nT_x$ (n = 1–3), in which M, X, and T_x denote a transition metal (e.g., Ti, Zr, Hf, V, Nb, Ta, Cr, or Mo), C and/or N, and surface termination groups (e.g., -OH, -O, or -F) [73,74], respectively. Unique structure of inner conductive matrix and pre-intercalated water, MXene enables fast electron supply and fast ion transport, which over 80% electrochemical performance maintain at very high scan rates ranging from 10 to 100,000 mV s^{-1} [29]. However, a major change is inseparable from its different exfoliation strategy. $Ti_3C_2T_x$ MXene can be made by selective etching of certain atomic layers from their layered precursors. F-containing acidic solutions or *in situ* formation of HF have been predominantly used as two typical routes [27,75]. In addition, a variety of alternative synthesis methods have been developed, including electrochemical etching [76], alkaline etching [77], molten salt etching [78], and halogen etching [79], to obtain MXene materials with controllable surface chemical properties and structural characteristics.

3.1. HF Etching

In 2011, Gogotsi group [27] successfully produced accordion-like Ti_3C_2 through selective extraction of Al from the Ti_3AlC_2 MAX phase in concentrated hydrofluoric acid (HF) solution (50%) (Figure 3a). During this process, removal of the Al atomic layers was accompanied by the introduction of surface terminations such as -F, -O, and -OH, giving rise to the characteristic surface chemistry of $Ti_3C_2T_x$. The underlying etching and functionalization reactions can be represented by the following equations [27]:

$$Ti_3AlC_2 + 3HF = AlF_3 + 3/2H_2 + Ti_3C_2 \quad (2)$$

$$Ti_3C_2 + 2H_2O = Ti_3C_2(OH)_2 + H_2 \quad (3)$$

$$Ti_3C_2 + 2HF = Ti_3C_2F_2 + H_2 \quad (4)$$

As shown in Equations (2)–(4), the MAX precursor reacts with HF to yield the target MXene and fluoride species, accompanied by H_2 release. The resulting multilayered MXene bears various surface terminations (-OH, -F, and -O), which render it highly hydrophilic (Equations (5) and (6)). Subsequently, HF etching method is successfully implemented in other types of precursor MAX phases, yielding many new MXene, i.e., Ti_2CT_x, V_2CT_x, Nb_2CT_x, $(Ti_{0.5}Nb_{0.5})_2CT_x$, $Mo_{4/3}CT_x$, etc. [80–84].

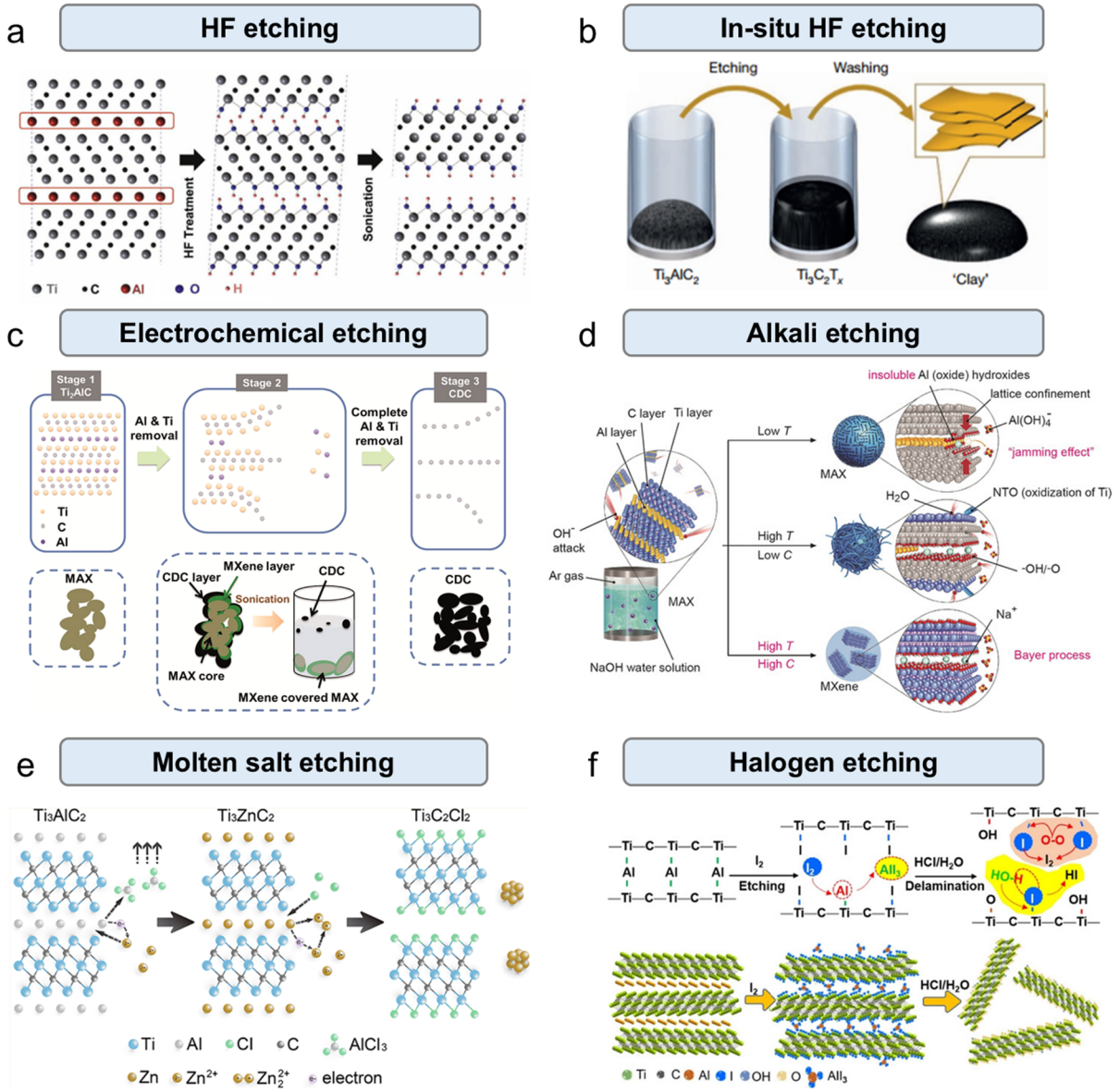

Figure 3. Synthesis method of $Ti_3C_2T_x$ MXenes. (**a**) HF etching. Reprinted with permission from Ref. [27]. Copyright 2011, Wiley-VCH. (**b**) *In-situ* etching. Reprinted with permission from Ref. [75]. Copyright 2014, Nature. (**c**) Electrochemical etching. Reprinted with permission from Ref. [76]. Copyright 2017, Royal Society of Chemistry. (**d**) Alkali etching. Reprinted with permission from Ref. [77]. Copyright 2018, Wiley-VCH. (**e**) Molten salt etching. Reprinted with permission from Ref. [78]. Copyright 2019, American Chemical Society. (**f**) Halogen etching. Reprinted with permission from Ref. [79]. Copyright 2021, American Chemical Society.

3.2. In-Situ HF Etching

The severe corrosiveness and toxicity of concentrated HF, together with the safety hazards and environmental concerns associated with its use, have hindered MXene fabrication and advancement to some extent [85]. This has motivated the development of etching strategies that are safer and more eco-friendly. In 2014, Ghidiu et al. [75] first synthesized high-quality $Ti_3C_2T_x$ MXene conductive clay by using the mixed solution of hydrochloric acid (HCl) and lithium fluoride (LiF), which can be fabricated into flexible films via roller pressing and directly used as electrode materials. The MXene film exhibits remarkable flexibility, toughness, and hydrophilicity, allowing it to be readily shaped into an "M" configuration while preserving an electrical conductivity of 1500 S cm^{-1} (Figure 3b). During etching, HF is generated *in situ* to attack the MAX phase, thereby eliminating the need for direct HF handling and substantially mitigating safety hazards in MXene synthesis. Meanwhile, Li^+ and H_2O molecules are able to intercalate into the interlayer space of MXene, thereby enlarging the interlayer distance [86]. In addition, the MAX phase can also be etched by fluoride salts (LiF, NaF, KF, or NH_4F) combined with an acid such as H_2SO_4 [87,88].

3.3. Electrochemical Etching

The traditional fluorine-containing etching method usually introduces -F functional groups onto the surface of MXene, which may have an adverse effect on its electrochemical properties in certain systems [89]. Accordingly, the development of safer, efficient, and fluorine-free synthetic routes has become increasingly important [90]. Electrochemical etching has emerged as an alternative route for MXene production, in which the MAX phase undergoes anodic treatment under an applied potential to selectively dissolve the Al layers. Sun and co-workers [76] used low-concentration HCl solutions to etch Ti_2AlC by electrochemical etching for the first time, resulting in a trilayer structural composite consisting of MXene, carbon-derived carbides (CDCs) and unetched MAX. The mechanism and schematic illustration of the electrochemical etching process are presented in Figure 3c, where the CDCs layers are located on the MAX surface, limiting further etching and causing the formation of a MXene covered MAX. There is no fluorine ion involved in the electrochemical etching process, so the generated MXene only contains -Cl, -O and -OH functional groups. Furthermore, the authors also found that the electrochemical properties of MXene were boosted owing to the -Cl terminal group introduction. Thus, the functional groups can be controlled by electrochemical etching methods to improve the properties of MXene. Subsequently, Yang et al. developed a binary aqueous electrolyte composed of NH_4Cl and tetramethylammonium hydroxide (TMAOH), enabling the preparation of $Ti_3C_2T_x$ nanosheets with lateral dimensions of up to 18.6 μm and a production yield exceeding 90% [91].

3.4. Alkali Etching

Although acid solution is generally utilized in the traditional synthesis of MXene, Aluminum is amphoteric with stronger ability to combine with alkali, so it is theoretically feasible to prepare high-purity MXene by alkali etching [92]. Recently, Li et al. [77] prepared $Ti_3C_2T_x$ in high yield through an alkali-assisted hydrothermal treatment (27.5 M NaOH, 270 °C; Figure 3d). Under high-temperature and high-pressure conditions, concentrated NaOH rapidly attacks the Al layers, oxidizing Al to aluminum oxide or hydroxide; these species then dissolve in the alkaline medium, thereby etching Ti_3AlC_2. Notably, the resulting MXene is free of -F terminations, which benefits the overall performance of supercapacitors [93].

3.5. Molten Salt Etching

Compared with the alkali etching method, which involves adjusting the temperature and the concentration of NaOH, Lewis acidic molten salt etching offers improved safety and lower energy consumption, making it better suited to scalable MXene synthesis [94]. For instance, Li et al. [78] introduced a $ZnCl_2$/NaCl/KCl molten-salt system for MXene synthesis, in which Zn species generated from molten $ZnCl_2$ facilitated the selective removal of Al layers from the MAX phase (Ti_3AlC_2, Ti_2AlC, Ti_2AlN, and V_2AlC), as illustrated in Figure 3e. In this case, $ZnCl_2$ acted as an etchant, while the molar ratio of NaCl and KCl = 1:1 forms a molten salt bath to decrease the melting point of the eutectic system. The reaction mechanism can be depicted as follows [78]:

$$Ti_3AlC_2 + 1.5ZnCl_2 = Ti_3ZnC_2 + 0.5Zn + AlCl_3 \quad (5)$$

$$Ti_3ZnC_2 + ZnCl_2 = Ti_3C_2Cl_2 + 2Zn \quad (6)$$

Unlike fluoride-based molten salt etching, etching the MAX phase with a fluorine-free Lewis acid molten salt yields MXene surfaces free of electrochemically inactive -F groups [95]. Moreover, the resulting -Cl terminations have been reported to enhance electrochemical performance, which highlights the advantage of the Lewis acid molten salt etching route.

3.6. Halogen Etching

Recently, Shi et al. [79] reported a new route to accordion-like MXene via iodine etching (IE) in anhydrous CH_3CN, in which the resulting AlI_3 was subsequently removed with HCl solution. Notably, reacting the MAX phase with I_2 produced fluorine-free MXene bearing -I surface terminations (Figure 3f). In this regard, Jawaid et al. [96] prepared Ti_3C_2 MXenes with uniform Cl, Br, or I terminations by etching Ti_3AlC_2 with halogen-based etchants (Br_2, I_2, ICl, and IBr). Compared with the Lewis acid molten salt method, which demands high temperature requirements, this protocol has milder and safer conditions and enables synthesis under room temperature [97]. The halogen etching method not only offers more options to adjust the surface terminations of MXene, but also offers more insight into the etching mechanism of MXene [98].

4. Intrinsic Properties of $Ti_3C_2T_x$ Nanosheets

4.1. Morphological and Structural Characteristics

The electrochemical performance of MXene is closely related to its morphology, lateral size, thickness, and internal structure [99]. These factors collectively influence the accessibility of electrochemically active sites, as well as the transport of electrons and electrolyte ions [100]. In particular, the lateral size of MXene nanosheets significantly affects both electrode assembly and charge-storage behavior. Large nanosheets generally provide longer continuous pathways for electron transport and favor intersheet contact during fiber formation. They also facilitate liquid-crystalline ordering during wet spinning; for example, Zhang et al. [35] reported that large MXene flakes could form liquid-crystalline phases at much lower concentrations than smaller flakes. However, densely packed large nanosheets may restrict ion penetration into the inner regions of the electrode. In contrast, smaller nanosheets can shorten ion transport pathways and expose more edge active sites, but excessive fragmentation may introduce structural defects and increase interflake contact resistance [101]. Therefore, controlling the size distribution is crucial for balancing electronic conductivity and ion accessibility. Furthermore, the shape and stacking arrangement of MXene nanosheets strongly influence their electrochemical kinetics. Flat nanosheets tend to overlap and restack during drying and assembly. Although dense packing can contribute to high volumetric capacitance, excessive restacking reduces the accessible surface area and limits electrolyte penetration [102]. Introducing wrinkles, pores, or suitable interlayer spacers can help maintain open ion transport channels. Recent work has shown that incorporating smaller $Ti_3C_2T_x$ flakes between larger nanosheets can effectively reduce restacking and improve ion transport within MXene fiber electrodes. This structural design improves the utilization of active sites while preserving continuous conductive pathways. In addition to nanosheet morphology, interlayer spacing and orientation play important roles in determining electrochemical performance. Narrow interlayer channels may restrict ion insertion, whereas excessively loose structures can reduce packing density and weaken electrical contact between nanosheets. Li et al. [37] demonstrated that highly oriented $Ti_3C_2T_x$ fibers with regulated interlayer interactions achieved a remarkable volumetric capacitance of 1360 F cm^{-3}, highlighting the importance of controlling nanosheet arrangement and ion transport pathways. Furthermore, surface terminations affect electrolyte wettability and reversible redox reactions [65]. Overall, optimizing MXene electrodes requires a coordinated control of nanosheet dimensions, stacking structure, interlayer spacing, and surface chemistry, rather than maximizing any single structural parameter.

4.2. Dispersion Stability

Stable and homogeneous dispersions are fundamental to the solution processing of MXene-based fibers. Unlike many conventional 2D materials, $Ti_3C_2T_x$ MXene possesses abundant polar surface terminations (-O, -OH, and -F) introduced during MAX-phase etching (Figure 4a) [103]. These groups render MXene hydrophilic and govern its interfacial interactions with solvents [104]. In aqueous media, the electrostatic repulsion between negatively charged nanosheets suppresses premature aggregation, yielding stable colloidal dispersions. However, the dispersion state is highly sensitive to surface chemistry, nanosheet dimensions, pH, ionic strength, and solvent composition [105]. Solvent selection is particularly critical (Figure 4b). MXene generally exhibits favorable dispersibility in polar protic and aprotic solvents (e.g., water, DMSO, DMF, NMP) due to the matching of surface polarities, whereas it aggregates in nonpolar media [106]. Thus, choosing a dispersion medium requires balancing colloidal stability with compatibility for subsequent spinning and coagulation processes. Importantly, colloidal stability does not guarantee chemical stability. Prolonged exposure to dissolved oxygen and water inevitably leads to oxidative degradation, resulting in structural damage and conductivity loss. As demonstrated by Habib et al., [69] the visual appearance of MXene dispersion is not a reliable indicator of its oxidation state. Therefore, strictly controlling the storage environment (e.g., degassing, low-temperature storage) and minimizing oxygen exposure are crucial for maintaining the intrinsic properties of MXene prior to fiber assembly [107].

4.3. Rheological Properties

The rheological properties of MXene dispersions are pivotal for continuous fiber spinning. Owing to their 2D geometry and high aspect ratio (defined as lateral size/thickness, Figure 4c), MXene nanosheets exhibit concentration-dependent viscoelasticity [36]. Dispersions with high aspect ratios readily form lyotropic liquid-crystalline (LC) phases at relatively low concentrations. As concentration increases, the system transitions from an isotropic state to a biphasic state, and eventually to an ordered nematic phase (Figure 4d). This structural evolution is the prerequisite for achieving macroscopic nanosheet alignment during spinning. The isotropic-to-nematic transition concentration is highly dependent on flake dimensions. As reported by Zhang et al. [36] large-

flake dispersions can form nematic phases at concentrations as low as ~26.5 mg mL^{-1}, whereas small flakes require a much higher concentration (~150 mg mL^{-1}) to achieve a similar state. Furthermore, concentrated MXene dispersions typically exhibit shear-thinning behavior-a decrease in viscosity under shear-which facilitates extrusion through narrow spinnerets while simultaneously aligning the nanosheets along the flow direction. Beyond viscosity, the storage modulus (G′) and loss modulus (G″) are critical for evaluating spinnability. By mapping the G′/G″ ratio across different concentrations and frequencies, Akuzum et al. [108] constructed a rheological processing map (Figure 4e,f) that delineates the optimal windows for various manufacturing techniques, including electrospraying, inkjet printing, and wet spinning. A delicate balance is required: insufficient structural cohesion leads to filament breakage, while excessive elasticity hinders uniform extrusion. It should be noted that the G′/G″ ratio alone cannot fully predict spinnability, as coagulation kinetics and extrusion parameters also play vital roles in fiber continuity [109]. Overall, rational regulation of dispersion rheology is essential for bridging the gap between fundamental MXene properties and macroscopic fiber fabrication.

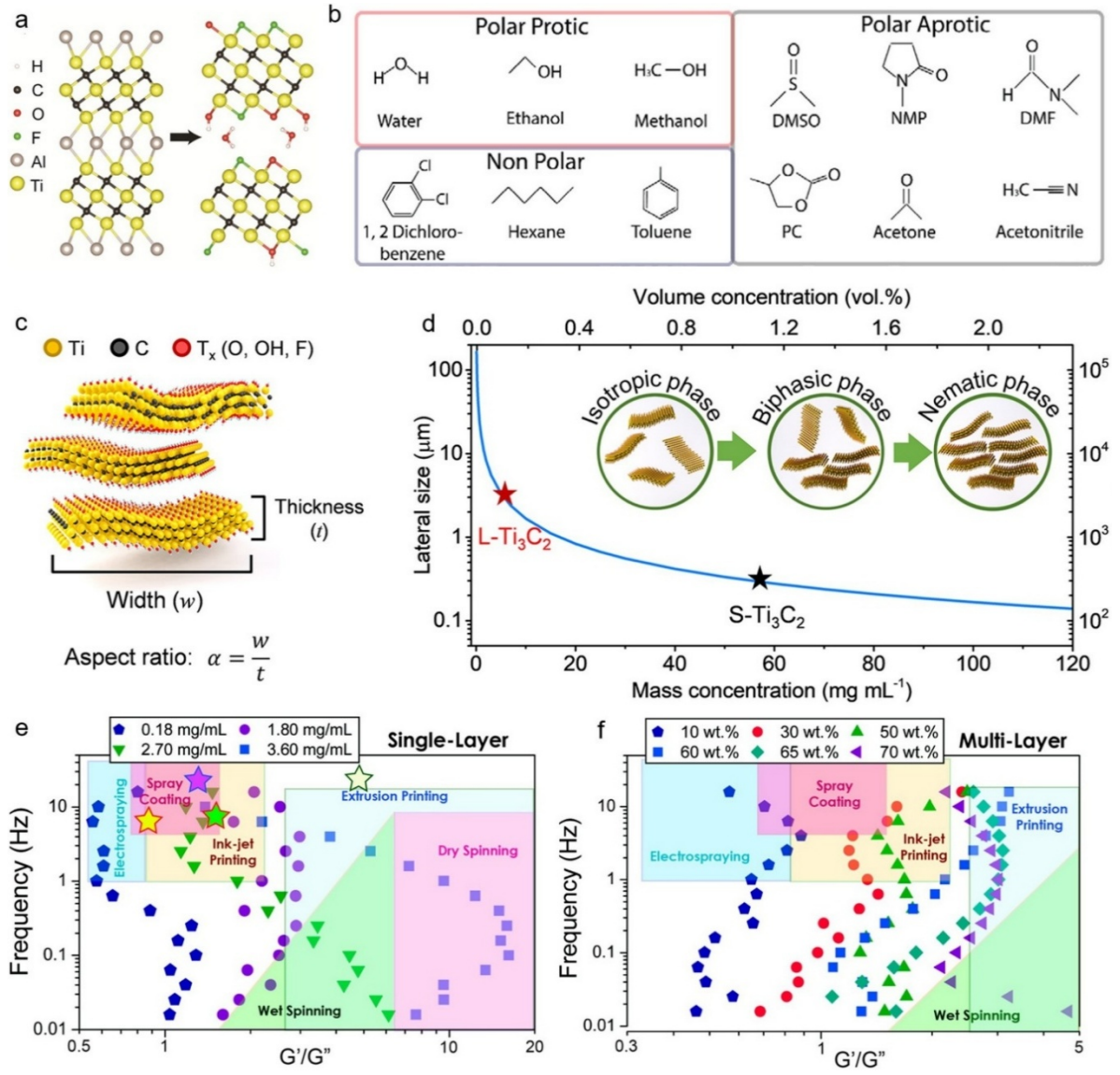

Figure 4. Intrinsic properties of MXene governing dispersion, liquid crystal formation, and rheological processing. (**a**) Atomic structure and surface terminations of $Ti_3C_2T_x$. Reprinted with permission from Ref. [103]. Copyright 2016, Royal Society of Chemistry. (**b**) Classification of solvents used for MXene dispersion. Reprinted with permission from Ref. [106]. Copyright 2017, American Chemical Society. (**c**) Schematic illustration of the nanosheet aspect ratio. (**d**) Phase diagram showing the isotropic-to-nematic transition for large and small MXene flakes. The red and black stars represent L-Ti_3C_2 and S-Ti_3C_2, respectively. Reprinted with permission from Ref. [36]. Copyright 2020, American Chemical Society. (**e**,**f**) Rheological processing maps (frequency vs. G′/G″) for single-layer and multi-layer MXene dispersions, respectively, guiding different processing techniques. The stars show the approximate processing parameters reported in the literature for various MXene applications. Reprinted with permission from Ref. [108]. Copyright 2018, American Chemical Society.

5. Fabrication of MXene-based Fabrics, Yarns and Fibers

5.1. Coating

Coating is a straightforward and potentially scalable strategy for incorporating MXene into existing fibrous substrates, including individual filaments, conventional yarns, and textile structures. Common approaches include dip coating, spray coating, and other solution-based deposition methods [110–112]. Compared with techniques that require the assembly of MXene nanosheets into self-supporting fibers, coating allows the original fiber morphology and mechanical support of the substrate to be largely retained while introducing an electrically conductive and electrochemically active surface layer [113]. The MXene loading and coating uniformity can be adjusted through the dispersion concentration, deposition cycles, and surface characteristics of the underlying fibers. For example, Uzun et al. [114] developed MXene-coated cellulose yarns with an MXene content of approximately 77 wt% and an electrical conductivity of up to 440 S cm^{-1}. The resulting yarns exhibited favorable knittability and retained their conductive characteristics after repeated washing, demonstrating the potential of coating strategies for textile-compatible energy-storage electrodes. Subsequently, Levitt et al. [115] developed an automated coating approach to fabricate continuous MXene-coated cotton and nylon yarns, which were further processed into three-dimensional knitted energy-storage textiles, as illustrated in Figure 5a. The assembled textile supercapacitors exhibited an areal capacitance of up to 707 mF cm^{-2} at 2 mV s^{-1} in an aqueous H_3PO_4 electrolyte, illustrating the feasibility of integrating MXene-coated yarns into scalable textile architectures.

Nevertheless, the electrochemical and mechanical performance of coated yarns is strongly dependent on the adhesion between MXene nanosheets and the fiber substrate. Repeated bending, twisting, and mechanical abrasion may cause partial coating detachment, interrupt conductive pathways, and compromise long-term stability [116]. Furthermore, increasing MXene loading through repeated deposition may produce thicker and more densely stacked coatings, potentially reduce mechanical compliance and restrict electrolyte access to internal active sites [117]. Recent coating-assisted structural designs, including the integration of MXene with carbon nanotube networks followed by yarn assembly, provide opportunities to improve interfacial stability and charge transport [118]. However, the additional deposition and assembly steps increase processing complexity. Therefore, the practical advantages of coating strategies depend on achieving an appropriate balance among MXene loading, coating adhesion, electrical conductivity, mechanical flexibility, and manufacturing efficiency.

5.2. Electrospinning

Electrospinning offers a versatile platform for producing nanofibrous structures from polymer-containing precursor solutions [119]. By incorporating functional nanomaterials into the spinning solution, a wide variety of composite nanofibers with tailored physicochemical properties can be obtained. Examples include graphene oxide and pseudocapacitive nanomaterials such as MnO_2 and MoS_2 [120,121]. However, electroactive particles or flakes tend to agglomerate or restack in solution. This behavior impairs fiber spinnability. Therefore, it is essential to attain a stable homogeneous electrospinning solution, which is a necessary condition for large-scale device manufacturing. Recently, there have been many works about adding MXene into spinning solution to electrospin MXene composite nanofibers like $Ti_3C_2T_x$/chitosan nanofibers, $Ti_3C_2T_x$/polyvinyl alcohol (PVA) nanofibers and $Ti_3C_2T_x$/polyacrylonitrile (PAN) nanofibers [122]. The fabricated MXene composite fibers are challenging to utilize as SC electrodes since the MXene flakes are usually located in the polymer fibers, where surrounding polymer chains hinder electron transport and reduce the accessibility of electrochemically active surfaces. To address this limitation, the researchers carbonized electrospun PAN/MXene composite fibers to convert the insulating polymer matrix into conductive carbon, thereby facilitating electron transport and improving the electrical conductivity of the resulting fibers. Through adjusting the carbonization conditions, composite fibers with high conductivity and high MXene load were synthesized [123] (Figure 5b). Beyond conventional electrospinning and subsequent carbonization, integrating electrospinning with surface coating has emerged as an effective strategy for regulating the distribution of electroactive components and improving the electrochemical performance of MXene-based carbon nanofiber electrodes. For example, Mokhtari et al. [124] systematically investigated three different approaches for incorporating $Ti_3C_2T_x$ MXene into electrospun polyacrylonitrile (PAN) nanofibers, including direct incorporation of MXene into the spinning solution, dip coating of electrospun nanofibrous mats, and a combination of both strategies, followed by thermal stabilization and carbonization. The results revealed that incorporating MXene directly into the spinning solution favored the flexibility of carbon nanofiber mats, whereas surface coating reduced dimensional shrinkage and increased carbon yield during carbonization. Notably, the combined strategy achieved higher MXene loading, enhanced electrical conductivity, and improved pseudocapacitive performance. These findings highlight the importance of controlling the distribution and interfacial organization of MXene nanosheets within electrospun fiber architectures to achieve a

favorable balance between mechanical flexibility and electrochemical performance. In addition to the optimization of fabrication processes, the incorporation of hybrid fillers represents another promising approach for improving the electrochemical properties of electrospun nanofiber electrodes. For instance, Zhang et al. [125] developed ZIF-8@MXene/carbon nanofiber composite electrodes through electrospinning and carbonization, followed by laser patterning to construct micro-supercapacitors for wearable self-charging power systems. The incorporation of ZIF-8@MXene hybrid components increased the availability of electrochemically active sites and facilitated charge transport within the carbon nanofiber network. These studies highlight the potential of electrospinning for developing porous electrodes with improved ion accessibility. However, obtaining high MXene loading while maintaining uniform fiber morphology and effective electronic conduction remains challenging. Moreover, electrospinning generally requires polymer-containing precursor solutions, and subsequent stabilization and carbonization introduce additional processing steps. Although electrospun nanofibrous mats can exhibit favorable flexibility and electrochemical performance, their morphology and mechanical behavior differ substantially from those of continuous yarn electrodes. Therefore, the advantages of electrospinning should be evaluated with consideration of the intended device architecture rather than directly compared with conventional fiber-shaped supercapacitors.

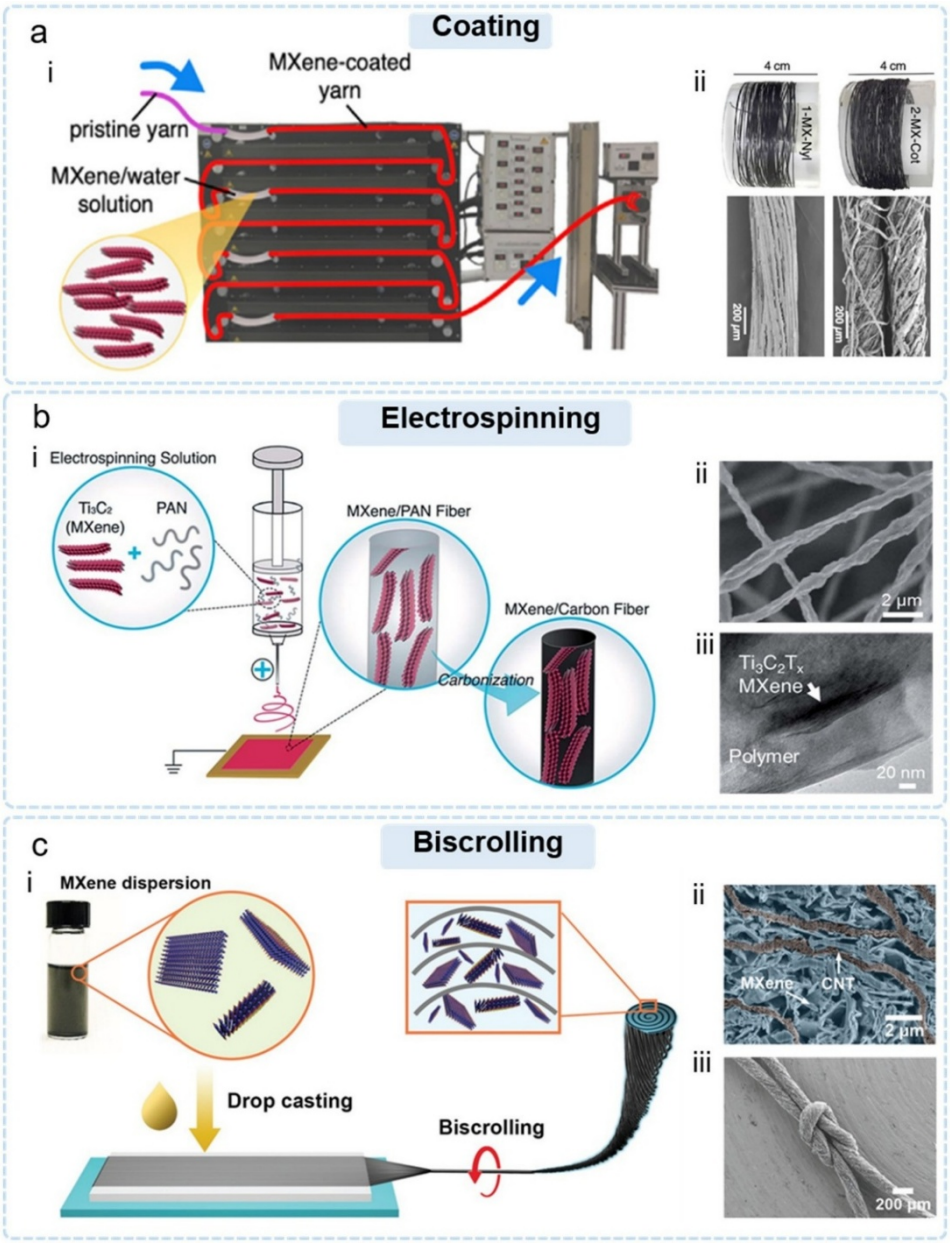

Figure 5. Methods for synthesising MXene-based fabrics, yarns and fibers. (**a**) Coating: (**i**) MXene-coated yarns. (**ii**) Optical and SEM images of MXene-coated cotton yarn and multifilament nylon fibers. Reprinted with permission from Ref. [115]. Copyright 2020, Elsevier. (**b**) Electrospinning: (**i**) MXene/PAN nanofibers; (**ii**) SEM images of electrospun PAN fibers; (**iii**) TEM image of 10 wt% MXene/8 wt% PAN. Reprinted with permission from Ref. [123]. Copyright 2019, Royal Society of Chemistry. (**c**) Biscrolling: (**i**) MXene/CNT yarns; (**ii**) High-

magnification color scanning electron microscope image showing MXene layers embedded in the carbon nanotube (CNT) framework. (**iii**) SEM image of a BMX yarn containing 90 wt% MXene tied into a reef knot. Reprinted with permission from Ref. [33]. Copyright 2018, Wiley-VCH.

5.3. Biscrolling

Biscrolling provides an alternative strategy for producing MXene-based yarn electrodes by incorporating electroactive nanosheets into a mechanically continuous carbon nanotube (CNT) scaffold [126]. In a typical process, MXene nanosheets are deposited onto CNT sheets through solution-based methods, followed by twisting and scrolling to form a composite yarn with a helical internal architecture, as depicted in Figure 5c. Unlike coating methods, in which MXene is primarily deposited on the external surfaces of existing fibers, biscrolling enables electroactive nanosheets to be distributed throughout the CNT yarn structure [127]. The interconnected CNT network serves as both a conductive framework and a mechanical support, while the helical arrangement provides internal spaces for accommodating MXene nanosheets and facilitating electrolyte penetration. Wang et al. [33] demonstrated the fabrication of MXene/CNT biscrolled yarns with an MXene loading approaching 90 wt%, while maintaining mechanical flexibility and favorable electrochemical performance. The resulting yarn electrodes exhibited a volumetric capacitance of approximately 1083 F cm^{-3} in an acidic electrolyte. This performance illustrates the effectiveness of incorporating highly concentrated electroactive components into conductive CNT frameworks. In comparison with conventional surface-coated yarns, biscrolling offers improved opportunities for high active-material loading and internal integration of MXene, while the CNT scaffold contributes to the structural integrity of the yarn [128]. Nevertheless, biscrolling also presents several limitations. The uniformity of MXene distribution, internal porosity, and electrical contact between adjacent components can be influenced by the CNT sheet structure, MXene deposition conditions, and applied twisting density. Excessive twisting or dense nanosheet packing may restrict ion transport, whereas insufficient structural consolidation can compromise mechanical integrity and electrical continuity [129]. In addition, the preparation of continuous CNT sheets and the controlled deposition and twisting processes increase manufacturing complexity, potentially limiting production throughput and reproducibility. Therefore, further improvements should focus on controlling MXene distribution, helical architecture, interfacial electrical contacts, and continuous yarn manufacturing. These considerations are particularly important for balancing high electrochemical activity with mechanical flexibility and large-scale processability.

5.4. Wet-Spinning

5.4.1. Wet-Spinning of MXene Fiber

Wet spinning serves as a scalable and continuous technique that enables the fabrication of long functional fibers [130]. The versatility of this technique has been demonstrated in the fabrication of conductive-polymer, carbon nanotube (CNT), and graphene-based fibers [131–133]. In a typical spinning process, the precursor dope is extruded through a spinneret into a coagulation medium, where solvent exchange induces continuous filament formation and solidification. The fibers are thereafter taken out of the bath, dried and continuously collected onto a winder. Similar to other two-dimensional colloidal materials such as graphene oxide (GO), MXene nanosheets possess abundant hydrophilic surface terminations, particularly -O and -OH groups, which promote stable dispersion in aqueous media. Such favorable dispersibility facilitates the formation of lyotropic liquid-crystalline (LC) phases at sufficiently high concentrations [134,135]. On the other hand, MXene also possesses a number of similar characteristics, such as liquid crystal behavior, pseudoplastic rheological properties, and dispersion in a variety of solvents, which permit the fabrication of pure MXene fibers by wet-spinning. For example, in the absence of additives, by adjusting the aspect ratio and concentration of MXene flakes, Zhang et al. [36] reported nematic LC MXene inks composed of large (3 μm) and small (300 nm) flakes at concentrations of about 26 and 150 mg mL^{-1}, respectively. These LC MXene inks were subsequently processed into continuous MXene fibers through wet spinning, as illustrated in Figure 6a, while Figure 6b shows a photograph of the resulting MXene fiber wound onto a spool. Compared to the acetic acid bath, MXene fibers fabricated using the chitosan coagulation bath presented a densely packed microstructure, as illustrated in Figure 6c,d. In addition, when the coagulation bath was chitosan aqueous solution, Ti_3C_2 fiber exhibited superb electrical conductivity (~7748 S cm^{-1}). Moreover, the pure Ti_3C_2 fiber possessed excellent volumetric capacitance about 1265 F cm^{-3}, which is on par with Ti_3C_2 film.

However, the critical challenge of wet-spinning neat MXene fibers is the weak interlayer interaction between MXene sheets, which makes the self-supporting structure easy to be destroyed. Thus, Han's group [136] developed a straightforward, additive/binder-free approach to successfully synthesize flexible and pure $Ti_3C_2T_x$ MXene fibers with meter-level length via large-scale wet-spinning assembly (Figure 6e). During the coagulation process, the introduction of ammonium ions successfully assembled MXene sheets into fibers with extremely high electrical

conductivity (7713 S cm^{-1}), whose cross-section was a highly dense nano lamellar structure, as illustrated in Figure 6f,g. However, MXene fibers tend to fracture under mechanical stress because of weak interactions between their building blocks and the limited length of these components. Therefore, enhanced electrostatic interactions between MXene nanosheets are very beneficial for the preparation of highly aligned fibers. They exploited a technique to boost the MXene gel network so that it is sufficiently stable to tolerate mechanical disturbances. The electrostatic interactions between MXene sheets can be effectively strengthened by tuning the pH. Because the MXene gel remains stable under external shear, the gel fibers spontaneously transform into highly aligned fibers under mechanical stretching during wet spinning (Figure 6h–j). Among the fiber samples, the highly oriented MXene fibers delivered the best overall electrical and mechanical performance, achieving a conductivity of 12,504 S cm^{-1} and a Young's modulus as high as 122 GPa [137].

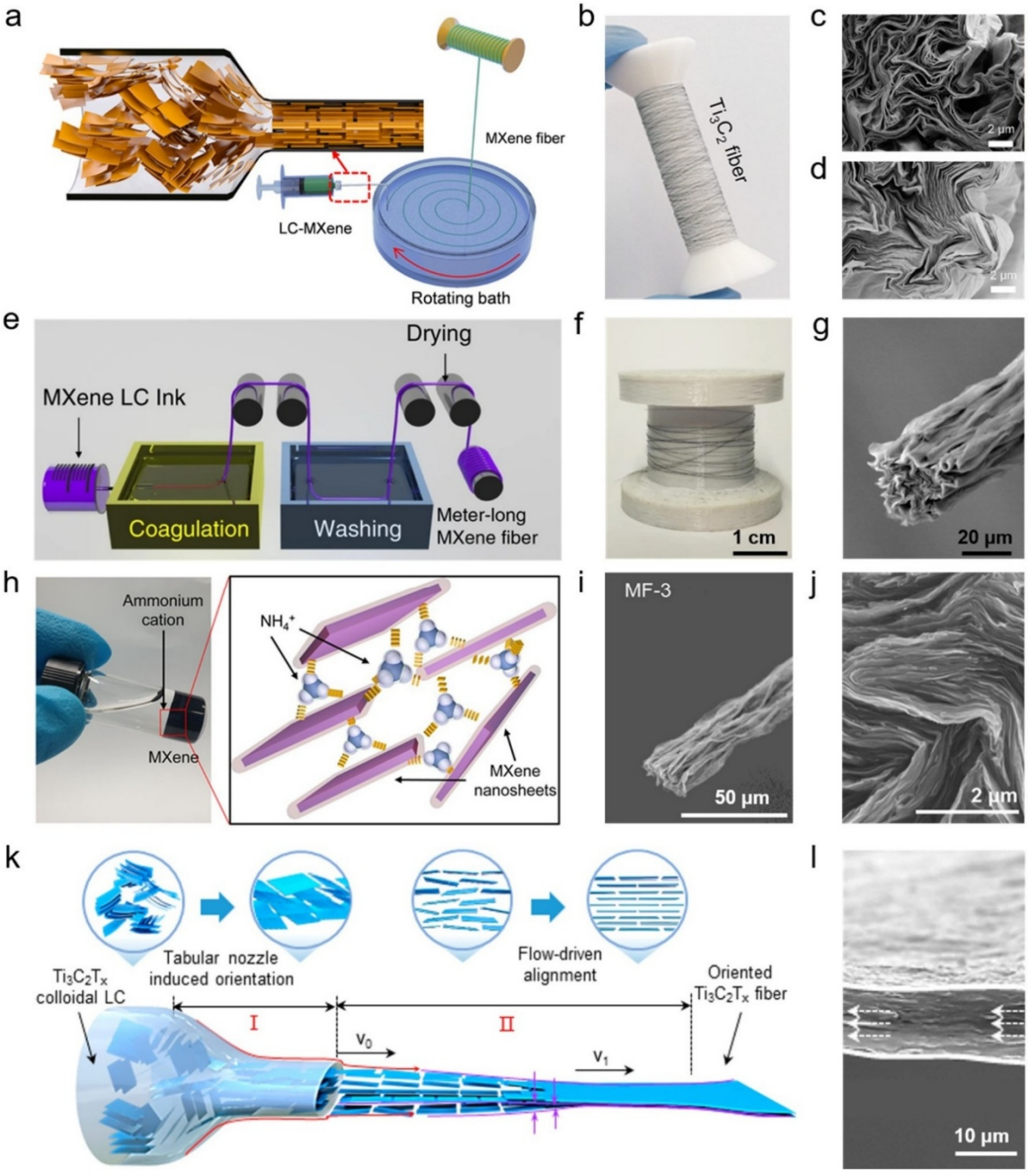

Figure 6. Fabrication of $Ti_3C_2T_x$ fibers by wet spinning. (**a**) Schematic illustration of pristine MXene fibers; (**b**) photograph of a pristine MXene fiber collected on a spool; (**c**,**d**) cross-sectional SEM images of MXene fibers prepared in acetic acid and chitosan baths, respectively. Reprinted with permission from Ref. [36]. Copyright 2020, American Chemical Society. (**e**) Schematic illustration of the $Ti_3C_2T_x$ MXene fiber; (**f**) $Ti_3C_2T_x$ MXene fiber wound on the bobbin; (**g**) SEM images of $Ti_3C_2T_x$ MXene fiber. Reprinted with permission from Ref. [136]. Copyright 2020, Springer Nature. (**h**) Optical images of gelled MXene in a vial and a scheme of the electrostatic interaction between MXene nanosheets during gelation; (**i**,**j**) SEM image of $Ti_3C_2T_x$ fiber. Reprinted with permission from

Ref. [137]. Copyright 2021, American Chemical Society. (**k**) Schematic illustration of the formation mechanism of highly oriented $Ti_3C_2T_x$ fibers. Stage I represents the initial orientation of $Ti_3C_2T_x$ nanosheets induced by the flat nozzle, while Stage II shows the further alignment along the fiber axis under the action of flow and stretching. The red arrows indicate the axial flow direction, and the purple arrows represent the lateral contraction of the fibers during the stretching process; (**l**) SEM image of the highly oriented $Ti_3C_2T_x$ fiber. Reprinted with permission from Ref. [37]. Copyright 2021, American Chemical Society.

The larger flakes of MXene tend to wrinkle and stack during the wet spinning process, resulting in structural defects that significantly reduce the mechanical and conductive properties of the fibers and impede the conduction of ions within the fiber structure, thus limiting the exploration of MXene fibers for applications such as sensing and energy storage [138]. Furthermore, under the action of external shear force, $Ti_3C_2T_x$ dispersion can form a directional liquid crystal structure and a two-dimensional sheet-oriented arrangement structure can be formed by means of wet spinning process. $Ti_3C_2T_x$ dispersions can form oriented liquid crystal structures under the action of external shear forces, and further can form two-dimensional lamellar oriented arrangement structures. With the benefit of this principle, Li et al. fabricated a highly oriented and densely packed $Ti_3C_2T_x$ fibrillar electrode through utilizing a tabular shaped spinning nozzle to induce flake orientation and fast flow-driven alignment. Magnesium ions serve as cross-linkers through electrostatic interactions, enabling the oriented $Ti_3C_2T_x$ fibers to exhibit good electrical conductivity (7200 S cm^{-1}) and tensile strength (118 MPa) [37], as shown in Figure 6k,l. Moreover, the fibers exhibited substantially improved charge-storage performance, delivering a volumetric capacitance of up to 1360 F cm^{-3}. This enhancement was attributed to the synergistic contribution of nanofluidic ion transport and Mg^{2+} intercalation-induced pseudocapacitance.

5.4.2. Wet-Spinning MXene-Based Composite Fiber

The incorporation of one-dimensional (1D) nanomaterials during wet spinning can strengthen intersheet interactions within MXene fibers and improve their structural integrity [139]. Beyond 1D additives, conductive polymers can also serve as effective interfacial binders. For example, poly (3,4-ethylenedioxythiophene):polystyrene sulfonate (PEDOT:PSS) has been introduced between MXene nanosheets to facilitate fiber formation while simultaneously enhancing interfacial cohesion and electrical transport in the resulting MXene/PEDOT:PSS hybrid fibers [35]. During fiber formation in the sulfuric acid coagulation bath, not only is excess PSS removed from the hybrid fibers, but both PEDOT and MXene are well aligned along the fiber axis, which facilitate the preparation of hybrid fibers with high electrical conductivity (1489.8 S cm^{-1}), as depicted in Figure 7a,b. Besides, combining with good pseudocapacitance of PEDOT:PSS, the hybrid fibers displayed a superb rate performance (614.5 F cm^{-3}) with ≈70 wt% of MXene. However, the synthesized $Ti_3C_2T_x$-based hybrid fibers often sacrifice flexibility to enhance capacitance, or conversely, the best balance between capacitive performance and flexibility remains challenging for hybrid fibers or devices assembled from these fibers. To achieve a favorable compromise between electrochemical performance and mechanical flexibility, Liu and co-workers [71] constructed $Ti_3C_2T_x$/aramid nanofiber (T/A) hybrid fibers via a wet-spinning strategy. Delaminated $Ti_3C_2T_x$ nanosheets served as the primary building blocks, while one-dimensional ANFs, derived from poly(p-phenylene terephthalamide) (PPTA) through proton donor-assisted deprotonation, were incorporated as flexible reinforcing components. The mixed dispersion was spun into a 0.5 M $FeCl_2$ coagulation bath, yielding hybrid fibers that combined good capacitive behavior with excellent flexibility (Figure 7c). At an ANF content of 5%, the resulting T/A-5 fiber achieved an effective balance between flexibility and mechanical robustness, exhibiting a tensile strength of 104 MPa, as shown in Figure 7d. Its high load-bearing capability was further demonstrated by its ability to lift a toy car.

Although FSCs have the advantages of light weight, being able to withstand various deformations, and the ability to withstand a wide range of working temperatures, due to the limitations of the design and production of fibrous electrodes, the energy density of FSCs is low, which hinders its practical applications. Consequently, novel fabrication strategies are urgently required to construct MXene-based fibrous electrodes that combine a high specific surface area with suitable porosity. In this context, Lee et al. [140] prepared MXene ($Ti_3C_2T_x$)/PAN fibers through a facile wet-spinning route, followed by carbonization, yielding hierarchically porous, freestanding carbon fibers (W-MX/CF) for use as negative electrode materials. Subsequently, ultrathin $NiCo_2S_4$ nanosheets were electrodeposited onto W-MX/CF to form $NiCo_2S_4$@WMX/CF, which served as the positive electrode for constructing an asymmetric FSSC (Figure 7e). Notably, both W-CF-50% and W-MX/CF-4 developed highly porous, interconnected architectures, providing abundant accessible sites for charge accumulation while establishing efficient pathways for ion transport (Figure 7f,g). The assembled device achieved a remarkable energy density of 40.70 mWh cm^{-3} at a power density of 301.51 mW cm^{-3}, demonstrating the feasibility of the FSSC as a high-performance power source for various electronic devices.

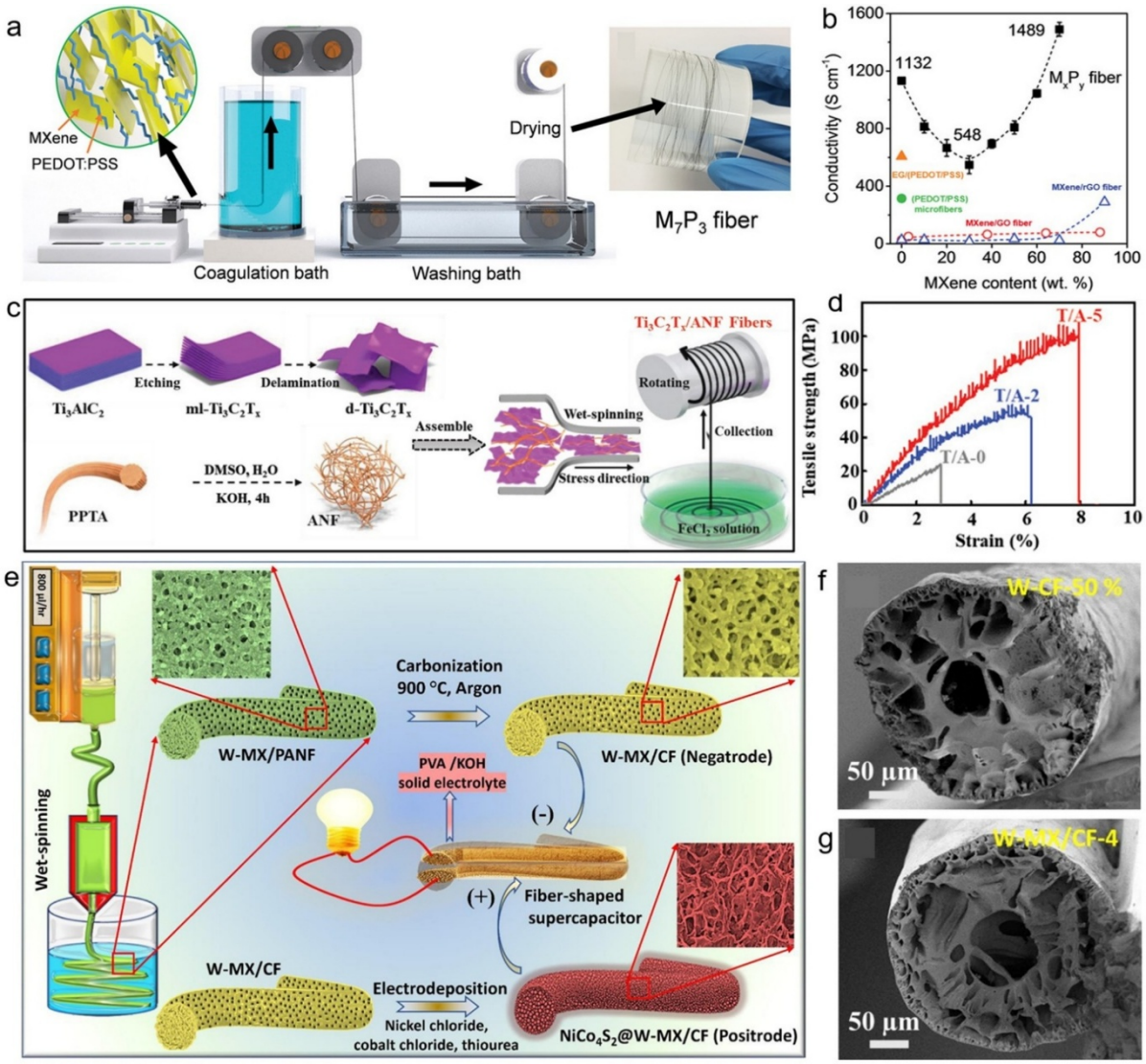

Figure 7. Schematic of wet-spinning MXene-based composite fiber. (**a**) MXene/PEDOT:PSS fiber; (**b**) Comparison of electrical conductivity. Reprinted with permission from Ref. [35]. Copyright 2019, Wiley-VCH. (**c**) $Ti_3C_2T_x$/ANF hybrid fibers; (**d**) tensile stress–strain curves of T/A fiber electrodes with varying ANF contents. Reprinted with permission from Ref. [71]. Copyright 2021, Wiley-VCH. (**e**) W-MX/CF and $NiCo_2S_4$@WMX/CF; Cross-sectional FE-SEM images: (**f**) W-CF-50% and (**g**) W-MX/CF-4. Reprinted with permission from Ref. [140]. Copyright 2022, Elsevier.

CNTs and graphene fibers present great potential for wearable applications due to their outstanding mechanical and electrochemical performance [141,142]. Remarkably, GO fibers prepared by wet spinning can now be successfully knitted into fabrics using conventional knitting machines. Combining MXene with nanomaterials such as graphene oxide is one of the effective strategies to achieve spinnability. Razal and co-workers [32] demonstrated the feasibility of processing MXene dispersions into continuous fibers by employing a graphene oxide liquid-crystal (LC)-assisted spinning strategy, enabling the fabrication of fibers composed predominantly of MXene (Figure 8a). The well assembly of MXene and graphene oxide nanosheets can hinder the restacking of both nanosheets and improve the structure of the fibers, resulting in higher electrical and mechanical behaviors. The MXene/GO fibers are able to withstand multiple bends without fracture or microstructural damage even when tied into knots, demonstrating superb flexibility (Figure 8b,c). Furthermore, the MXene/reduced (rGO) fibers exhibit good volumetric capacitance (341 F cm^{-3}) and energy density of 5.1 mW h cm^{-3}. It is worth noting that during the chemical or thermal treatment reduction of graphene oxide fibers, defects in the lattice structure occur, leading to a decrease in the electrical conductivity of the reduced graphene oxide flakes, which in turn leads to a decrease in the output power. Highly conductive MXene flakes have been added to reduced graphene oxide fibers in an effort to improve their energy and power performance. Despite these advances, the electrical conductivity of rGO/MXene hybrid fibers remains relatively limited. Further investigation is therefore required to clarify how fiber architecture and interfacial organization govern the electrical and overall functional performance of emerging hybrid fiber systems. Gao and co-workers [143] addressed two aspects of the fiber electrode system.

The first issue involves elucidating the role of MXene sheet dimensions in governing the mechanical robustness and electrochemical characteristics of hybrid fiber architectures. The second involves how the liquid electrolyte within the fibers modulates their behavior. In this case, due to the binding effect of 60% mixed particle size MXene flakes, the rGO/MXene fibers with carefully engineered hierarchical structures possess superior mechanical performance and electrical conductivity (Figure 8d,e). In particular, the hybrid fibers achieved an electrical conductivity of 743.1 S cm^{-1}, a mechanical strength of 110.7 MPa, and a toughness of 3.8 MJ m^{-3} at 60% MXene loading. In addition, the effect of MXene size on the electrical conductivity of the hybrid fibers was also investigated, which is the large size and MXene loading of 50% of the hybrid fibers presented the best electrical conductivity. Moreover, the electrolyte mediated large-size MXene (L-MXene) fibers also showed better electrical conductivity.

Among 2D active materials, tungstate nanosheets offer intrinsic structural and functional benefits for fiber electrodes. (1) Their ultrathin morphology maximizes surface accessibility, enabling rapid ion transport over reduced diffusion distances while exposing numerous electrochemically active sites [144]. (2) The interconnected three-dimensional architecture facilitates electrolyte-ion penetration and shortens transport pathways, while providing abundant interfaces for pseudocapacitive reactions [145]. (3) Their large lateral dimensions and high aspect ratios further favor orientational ordering and continuous fiber formation during wet spinning [146]. On this basis, Li et al. [147] fabricated self-supporting axially aligned tungstate/MXene fibers through a mixed liquid-crystalline wet-spinning process. Within the hybrid fiber, two-dimensional tungstate nanosheets are integrated with MXene through electrostatic interactions, giving rise to a well-oriented sheet-on-sheet configuration. This hierarchical architecture combines the interconnected porous channels of tungstate for efficient ion migration with the highly conductive MXene network for rapid electron transfer, while the axial alignment further minimizes transport tortuosity. These synergistic structural features endow the tungstate/MXene fibers with favorable pseudocapacitive behavior, including high reversible charge-storage capability, excellent rate response, and remarkable mechanical flexibility. Furthermore, devices based on these hybrid fibers maintained sufficient energy output to operate LEDs, digital timers, thermo-hygrometers, and smart wristbands even when subjected to pronounced mechanical deformation (Figure 8f).

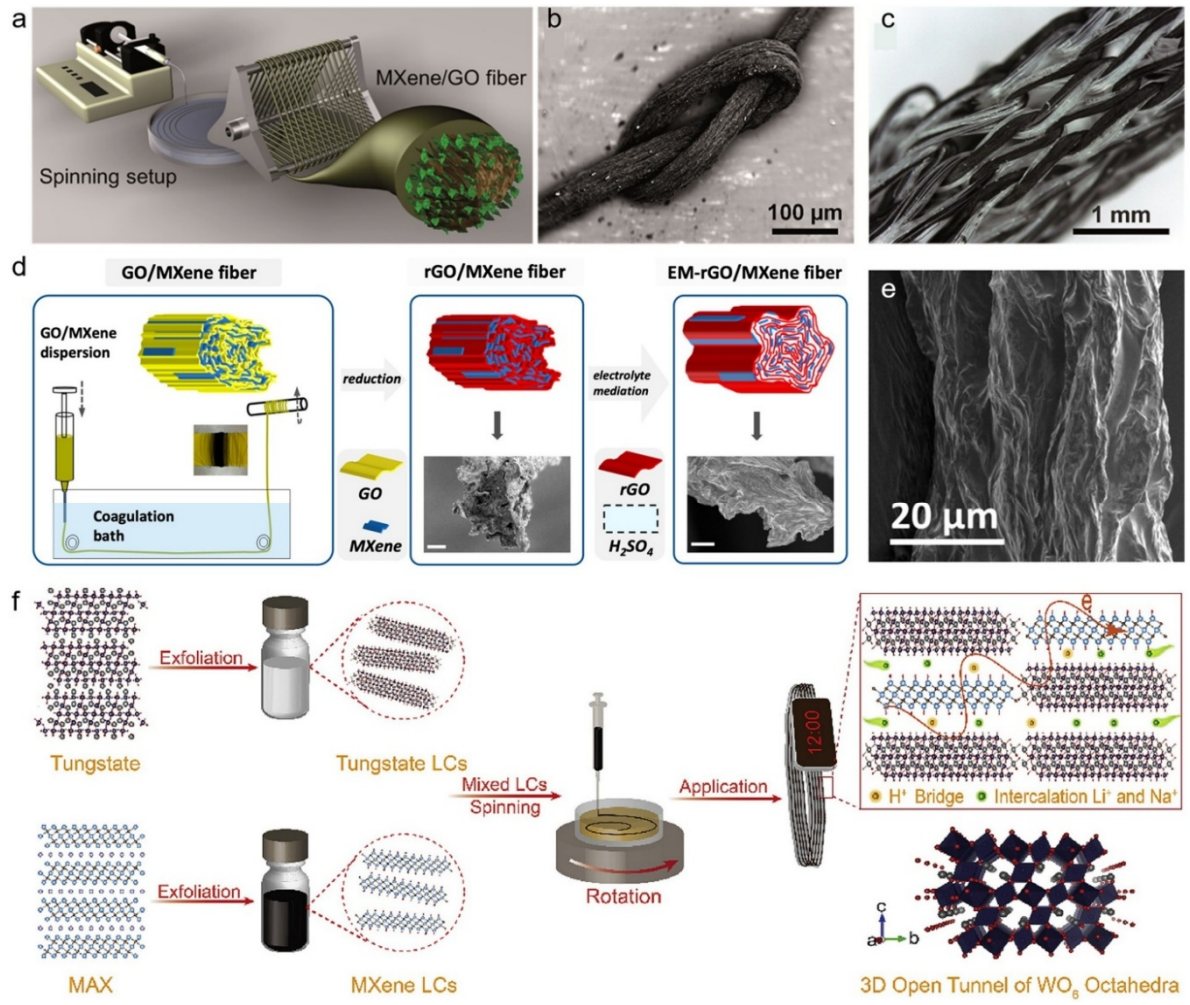

Figure 8. Schematic of wet-spinning MXene-based composite fiber. (**a**) MXene/GO fiber; (**b**) SEM image of a knotted MXene/GO fiber; (**c**) Optical image of an MXene/GO fiber textile prototype co-knitted with nylon yarn.

Reprinted with permission from Ref. [32]. Copyright 2017, Royal Society of Chemistry. (**d**) rGO/MXene fiber; (**e**) SEM images of EM-rGO/MXene fiber. Reprinted with permission from Ref. [143]. Copyright 2020, American Chemical Society. (**f**) Tungstate/MXene fiber. Reprinted with permission from Ref. [147]. Copyright 2020, Elsevier.

Despite substantial progress, the environmental instability of MXene continues to hinder the practical deployment of MXene-based fibers, particularly under humid, thermally demanding, or otherwise harsh operating conditions where oxidation can lead to progressive performance deterioration [44]. In addition, fibers assembled solely from MXene nanosheets generally suffer from limited tensile strength and fracture resistance [148]. Coaxial wet spinning therefore provides an attractive structural-engineering strategy, allowing mechanically robust components to be integrated with functional MXene phases within a single fiber architecture and thereby improving the balance between mechanical durability and functional performance [149]. Compared with uniaxial fibers, coaxial architectures can achieve superior performance through core-sheath bonding. This advantage arises because incorporating conductive fillers into a polymer matrix often impairs spinnability (i.e., the ability to form fibers) and reduces the stretchability of the resulting fiber [150]. By comparison, core-sheath fiber design separates the conductive material into one layer (core or sheath) while keeping the polymer layer intact. A PU/MXene-PU core sheath structure can address the irreversible resistance increase under repeated stretching cycles [151] (Figure 9a,b). To demonstrate their potential in wearable applications, the researchers wove MXene/PU core-sheath fibers into a one-piece elbow sleeve. This sleeve is capable of tracking various elbow movements of the wearer, as illustrated in Figure 9c. Subsequently, Liu et al. [38] employed a coaxial wet-spinning strategy to construct ANF@M fibers with a well-defined core-shell architecture. As illustrated in Figure 9d, the highly conductive MXene core was encapsulated by a mechanically robust ANF sheath. This hierarchical configuration endowed the resulting fibers with exceptional strength and toughness, together with high electrical conductivity and enhanced resistance to environmental degradation. Negatively charged MXene flakes were effectively cross-linked together by NH^{4+} ionic electrostatic interactions in a coagulation bath of NH_4Cl (5 wt%) in aqueous solution. The mechanical performance of the fibers is strongly governed by their core–shell architecture and component organization. Benefiting from the highly oriented structure, the ANF@M fibers achieved a tensile strength of 502.9 MPa and an exceptional toughness of 48.1 MJ m^{-3}, both substantially exceeding those of pristine MXene fibers (Figure 9e). A typical core–shell structure without obvious interfacial delamination is observed in cross-sectional SEM images of ANF@M fibers, confirming strong interfacial adhesion between the MXene core and the ANF shell. Furthermore, the solid shell exhibits a large number of highly stretched and axially aligned microfibrils (Figure 9f–h). Excitingly, a core-shell fiber can not only support the cyclic rotation of a weight weighing 100 g, but also can be freely folded, spirally wrapped around a glass rod and even knotted without breaking, confirming that this lightweight, highly conductive and ultra-strong $Ti_3C_2T_x$ MXene-based core-shell fibers have tremendous potential for wearable electronics (Figure 9i). To further improve energy storage capacity, the conductive material can be modified by chemical/electrochemical deposition or hydrothermal reaction. This approach provides a feasible way to form core-shell fibers. Microfluidic spinning technology also enables the construction of advanced fiber structures, including porous backbones and vertically aligned networks. Such hierarchical architectures establish continuous pathways for electron conduction while maintaining accessible channels for ion migration, thereby promoting rapid charge-transfer kinetics and improved electrochemical performance. On this basis, hierarchically organized ZIF-L(Zn)@$Ti_3C_2T_x$ MXene core–sheath fibers were constructed through a microfluidic assembly strategy that integrated ionic cross-linking with a spatially confined reaction process [152] (Figure 9j,k). Moreover, the fiber possesses superb electrical conductivity and mechanical elasticity, allowing easy lifting of 20 g (Figure 9l). In order to facilitate a comprehensive comparison of different preparation strategies, Table 1 summarizes the MXene content, preparation methods, electrical conductivity and mechanical properties of representative MXene-based fibers.

Table 1. Comparison of mechanical properties of MXene-based fibers.

Materials	MXene Content [wt%]	Preparation Method	Conductivity [S cm^{-1}]	Tensile Strength [MPa]	Young's Modulus [GPa]	Toughness [MJ m^{-3}]	Ref.
MXene/rGO	88	Wet spinng	72.3	116	13.3	0.94	[32]
$Ti_3C_2T_x$/CNT	90	Biscrolling	26	26.6	0.09	2.01	[33]
$Ti_3C_2T_x$/ PEDOT: PSS	70	Wet spinng	1489.8	58.1	7.5	0.32	[35]
$Ti_3C_2T_X$/Cellulose Yarns	77	Coating	440	468.4	5.06	-	[114]
$Ti_3C_2T_x$/ Nanoyarns	-	Electrospinning	1195	40	-	0.27	[153]
$Ti_3C_2T_x$/PU	23.1	Wet spinng	22.6	14	1.15	-	[151]

Table 1. *Cont.*

Materials	MXene Content [wt%]	Preparation Method	Conductivity [S cm^{-1}]	Tensile Strength [MPa]	Young's Modulus [GPa]	Toughness [MJ m^{-3}]	Ref.
$Ti_3C_2T_x$	100	Wet spinng	7713	63.9	29.6	0.09	[136]
$Ti_3C_2T_x$/ANF	95	Wet spinng	1025	104	-	-	[71]
$Ti_3C_2T_x$	100	Wet spinng	12503.8	343.7	122	0.48	[137]
GO/$Ti_3C_2T_x$@RC	70	Wet spinng	167.5	92.2	9	3.0	[154]
$Ti_3C_2T_x$/CNT	91	Wet spinng	1715	161	-	-	[155]
$Ti_3C_2T_x$/ polyrotaxane	-	Wet spinng	1000	500	-	60	[156]
MXene-silk	95	Wet spinng	3700	80		0.45	[157]
$Ti_3C_2T_x$/Kevlar	95	Thermal drawing	1412	242.6	31.8	1.0	[158]
$Ti_3C_2T_x$/sodium alginate (SA)	75	Immersion Rotary Jet Spinning	479.2	145.2	22.2		[159]
$Ti_3C_2T_x$-CMC	99	Wet spinng	1073	81			[39]
MXene-CDs	99	Wet spinng	2405	80			[160]
RSF/PEI/MXene	-	Wet spinng	1125	214.3	7.6	15.2	[40]

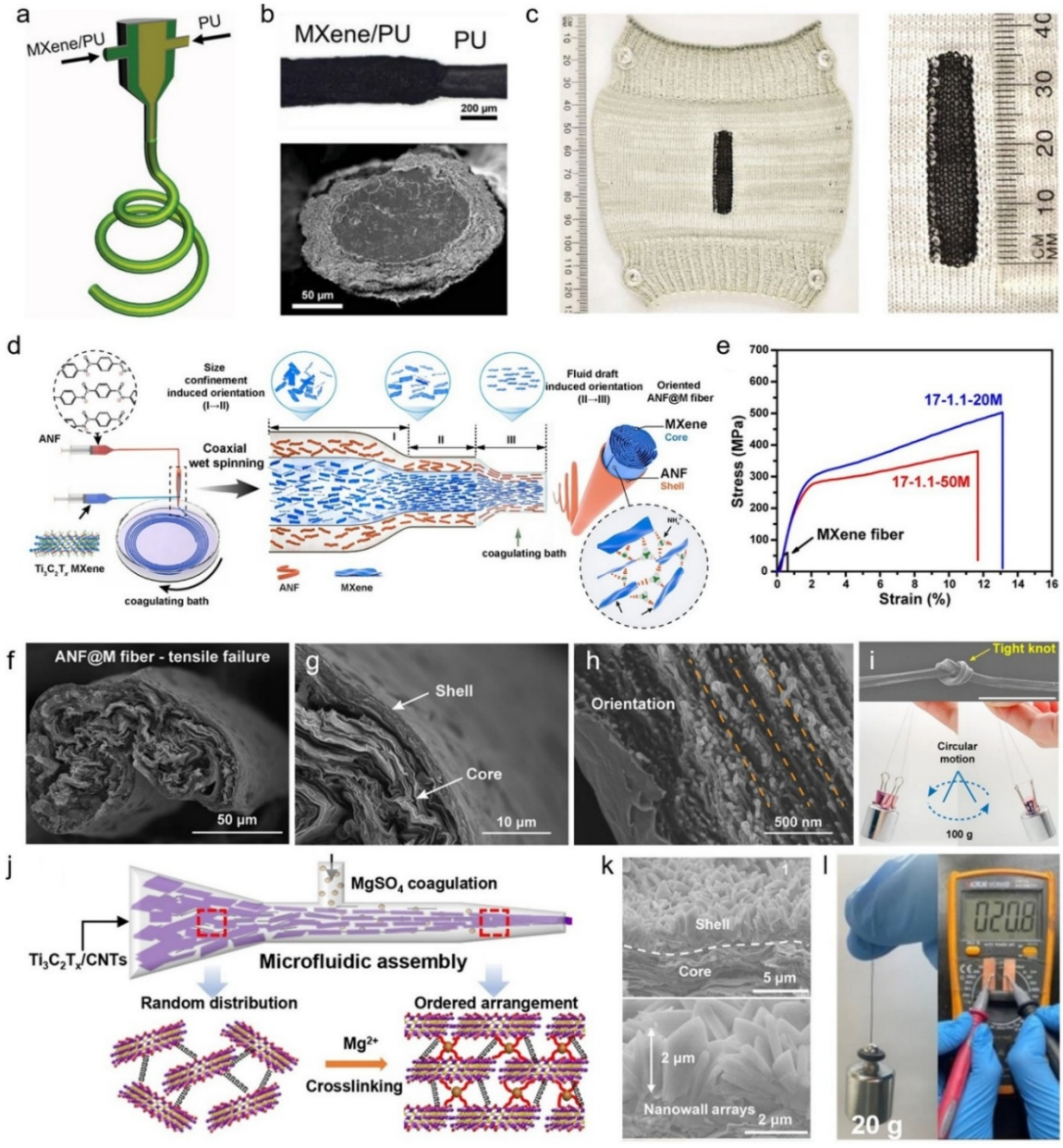

Figure 9. Wet spinning of coaxial MXene-based composite fibers. (**a**) MXene/PU fiber; (**b**) optical and SEM images of an MXene/PU coaxial fiber; (**c**) elbow sleeve knitted from four-ply MXene/PU composite yarn.

Reprinted with permission from Ref. [151]. Copyright 2020, Wiley-VCH. (**d**) ANF@M core-shell fibers; (**e**) Typical tensile stress–strain curves of ANF@M fiber; (**f**–**h**) SEM image of ANF@M fiber; (**i**) the fiber supports a 100 g weight during circular motion. Reprinted with permission from Ref. [38]. Copyright 2022, Springer Nature. (**j**) Microfluidic spinning assembly for hierarchical-ordered ZIF-L(Zn)@$Ti_3C_2T_x$ fibers; (**k**) SEM image of the ZIF-L(Zn)@$Ti_3C_2T_x$ fibers; (**l**) Fiber lifting 20 g weight, presenting a resistance of 20.8 Ω. Reprinted with permission from Ref. [152]. Copyright 2022, Wiley-VCH.

6. Applications of MXene-Based FSCs

Owing to their excellent flexibility, conformability, lightweight nature, and compatibility with textile processing, FSCs provide an attractive platform for the development of integrated and multifunctional energy systems [161]. To meet the growing requirements of wearable electronics, FSCs have been coupled with various functional components, including energy-harvesting units and sensing modules, enabling the construction of self-sustained and multifunctional wearable systems [162]. In this regard, all-pseudocapacitive asymmetric SCs were obtained via combining $Ti_3C_2T_x$ MXene as negative electrodes and aqueous RuO_2 electrodes as positive electrode on carbon cloth. By exploiting the complementary electrochemical potential ranges of MXene and RuO_2, an asymmetric RuO_2//$Ti_3C_2T_x$ supercapacitor was constructed, achieving an expanded operating voltage of 1.5 V, which is among the widest voltage windows reported for MXene-based supercapacitors [163], as shown in Figure 10a,b. Benefiting from the extended voltage range and synergistic electrode coupling, the assembled asymmetric device delivered a high energy density of 37 μWh cm^{-2} at a power density of 40 mW cm^{-2}, while maintaining outstanding cycling durability. To demonstrate the practical application potential of the device, two asymmetric devices were connected in series to construct a tandem in-plane device, which delivered an output voltage of up to 3 V. As shown in the inset of Figure 10c, the tandem device was able to power a 3 V light-emitting diode (LED). Subsequently, Shi et al. [164] reported a braidable coaxial FSC. In this architecture, a meter-long $Ti_3C_2T_x$ MXene cathode fiber serves as the core, while a zinc negative fiber acts as the sheath and is braided over the solid electrolyte coated on the MXene fiber surface (Figure 10d). The coaxial FSC delivered a capacitance of 214 mF cm^{-2} and a corresponding energy density of 42.8 μWh cm^{-2}. Figure 10e compares the cyclic voltammetry (CV) curves of the coaxial FSC under different bending curvatures/diameters. The shapes of the CV curves remain almost unchanged, indicating that the FSC possesses excellent flexibility, which is crucial for wearable energy storage devices. To further verify the stability of the coaxial FSC, three FSCs connected in series can simultaneously light up 12 red LEDs, as shown in Figure 10f. In addition to its high charge-storage capability, the device exhibited robust cycling durability and retained its capacitive performance under different bending conditions, demonstrating excellent electrochemical stability against mechanical deformation (Figure 10g). Furthermore, the high-performance FSC has a braided structure, giving it excellent stability and weavability. This allows it to be woven into a watch band or embedded in a textile (Figure 10h,i). The resulting device can power smart bracelet for several days, as shown in Figure 10j. Such performance illustrates the potential of wearable energy storage devices for large-scale production and practical application.

FSCs have emerged as attractive power sources for wearable electronic systems because of their intrinsic compatibility with textile architectures [165]. Their compact three-layer configuration facilitates weaving or braiding into fabrics and enables integration with other functional components without substantially compromising electrochemical performance or mechanical reliability [166]. Li et al. [37] utilized PAM/$MgSO_4$ gels as electrolytes to assemble MXene based fibers with high scale orientation into quasi-solid state FSCs, exhibiting outstanding mechanical flexibility under different bending angles (Figure 11a,b). The thus-prepared MXene-based FSC demonstrated a maximum volumetric energy density (10.61 mW h cm^{-3}) at a volumetric power density (212.2 mW cm^{-3}). Taking advantage of their mechanical flexibility, the FSCs were further woven into textile platforms. As shown in Figure 11c, the MXene fibers could be incorporated into textiles while maintaining flexibility under different configurations. Four FSCs connected in series and embedded within commercial gloves successfully powered a 3 V light-emitting diode while maintaining stable operation under repeated bending and stretching conditions (Figure 11d), highlighting their promise for flexible and wearable energy-storage systems. Considering these great properties, Han et al. fully integrated the as-prepared highly conductive $Ti_3C_2T_x$ MXene fiber into a wire and successfully powered a white LED. Beyond textile integration, the fiber was further employed as a functional component in a headphone cable, allowing signal transmission and illustrating its potential for miniaturized wearable and portable electronic applications [136] (Figure 11e,f). However, although considerable efforts have been devoted to improving the energy density of FSCs, a single fiber-shaped device still suffers from limited energy-storage capacity, which restricts its ability to independently power sophisticated wearable systems. To address this, Wu et al. [152] connected multiple FSC units in parallel to construct a chip-based supercapacitor (C-SC) capable

of powering demanding electronic devices (as described in Figure 11g). In addition, we designed an ambient-light-driven self-powered system consisting of a solar cell, the C-SC, and electronic devices. Upon solar illumination, the photovoltaic cell converts incident light into electricity, which can subsequently be stored in the coupled energy-storage unit. The generated electricity is then stored in the C-SC, which subsequently supplies power efficiently to electronic products once enough energy has been accumulated. After photovoltaic energy harvesting under ambient illumination, the generated electricity is stored in the C-SC and subsequently used to power practical electronic devices. The stored energy is sufficient to operate a water-level monitoring system equipped with both warning and illumination functions. In addition, the integrated self-powered platform can drive an earthquake alarm (Figure 11h,i), highlighting its applicability to emergency monitoring and electronic operation under disaster-related or harsh environmental conditions.

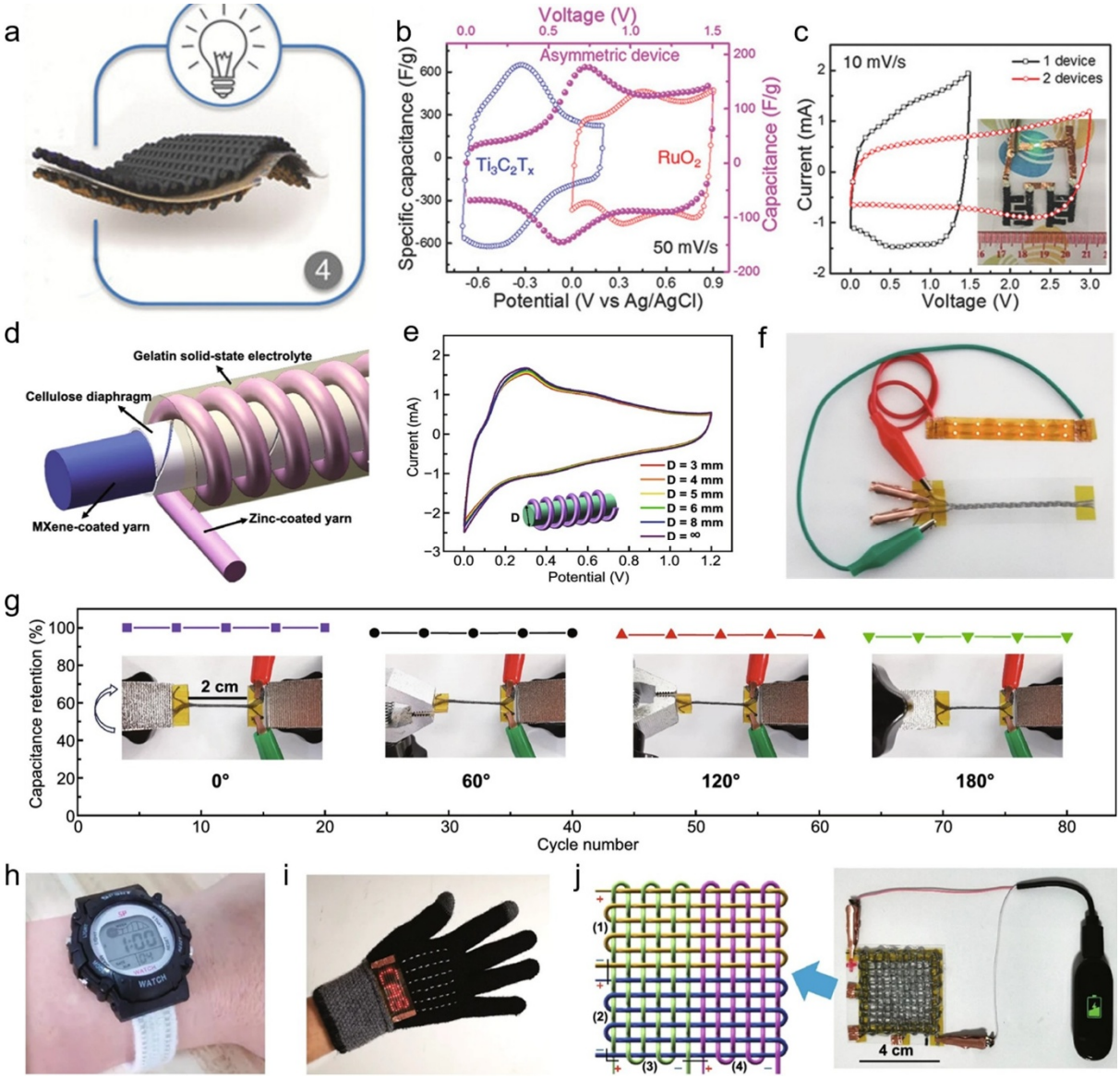

Figure 10. (**a**) RuO_2//$Ti_3C_2T_x$ asymmetric pseudocapacitor; (**b**) CVs of RuO_2/CF, $Ti_3C_2T_x$/CF and the asymmetric device; (**c**) The cyclic voltammogram of the RuO_2//$Ti_3C_2T_x$ series-in-plane device. The illustration shows that the two connected devices light up a green LED. Reprinted with permission from Ref. [163]. Copyright 2018, WILEY-VCH. (**d**) Structural diagram of wound coaxial FSC; (**e**) CV profiles of the coaxial FSC under different bending states; (**f**) A 12-LED array was powered by three SCs connected in series; (**g**) Capacitance retentions after twisting at various degrees; (**h**) Photograph of a sports watch powered by a textile bracelet composed of two coaxial FSCs; (**i**) The letters "CAS" formed by an array of 44 LEDs powered by six FSCs; (**j**) A smart bracelet charged by four series-connected FSCs. Reprinted with permission from Ref. [164]. Copyright 2021, Springer Nature.

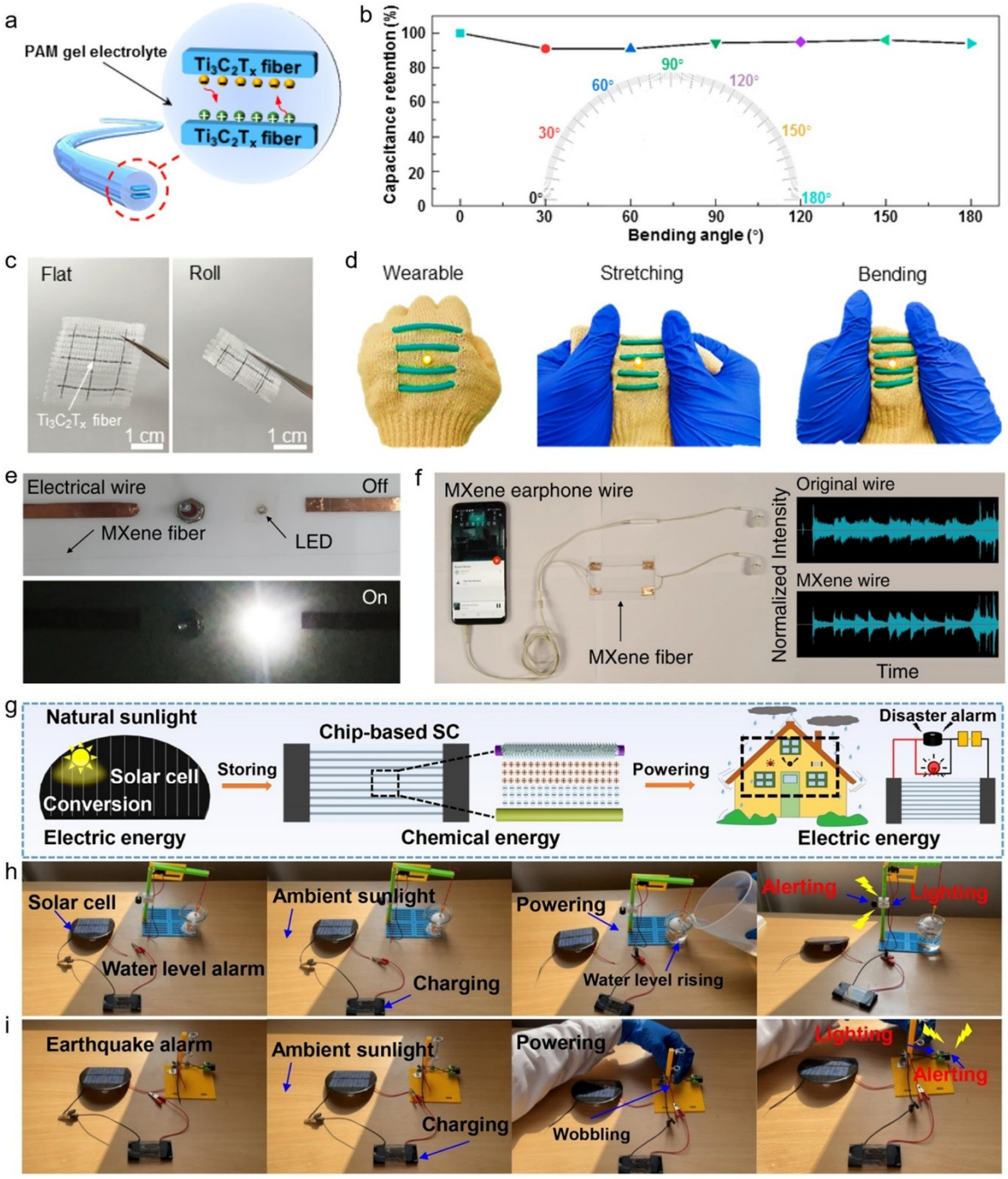

Figure 11. (**a**) Schematic of the fiber-shaped quasi-solid-state supercapacitor; (**b**) capacitance retention at various bending angles; (**c**) MXene fiber integrated in the textile; (**d**) Photographs of a glove incorporating four fiber-shaped supercapacitors. Reprinted with permission from Ref. [37]. Copyright 2021, American Chemical Society. $Ti_3C_2T_x$ MXene fiber applied as an electrical wire (**e**) and an earphone wire. (**f**) Reprinted with permission from Ref. [136]. Copyright 2020, Springer Nature. (**g**) Schematic of the self-powered system; (**h**,**i**) photographs of this system powering a water-level alarm and an earthquake alarm, respectively. Reprinted with permission from Ref. [152]. Copyright 2022, WILEY-VCH.

Although MXene-based FSCs have demonstrated promising performance in wearable electronics, their practical applicability depends on the power requirements and energy demands of the connected devices [167]. The high volumetric capacitance of MXene electrodes does not necessarily mean that a single FSC can provide sufficient energy for long-term operation [168]. The actual operating time depends on the total stored energy, usable voltage range, and power consumption of the electronic device. Regarding power requirements, the high electrical conductivity and pseudocapacitive charge storage of MXene electrodes enable rapid charging and high-power output, which are particularly beneficial for wearable sensors and communication modules. However, the actual operating time of a device depends not only on the normalized energy density but also on the total stored

energy and the power consumption of the electronics. For instance, while Li et al. [37] reported a high volumetric energy density of 10.61 mWh cm^{-3} for an MXene-based FSC, Shi et al. [164] demonstrated that two 3-cm-long MXene-based zinc-ion hybrid FSCs connected in series could power an electronic clock for approximately 110 min. This highlights that optimizing device configuration is just as important as enhancing the intrinsic electrode properties. In terms of energy density and device architecture, MXene does not always outperform carbon-based materials in every configuration. For example, Ahn et al. [21] compared asymmetric FSCs using graphene and MXene fibers paired with $CoNi_xO_\gamma$ electrodes. The graphene-based and MXene-based devices delivered volumetric energy densities of 76.15 and 48.57 mWh cm^{-3}, respectively. This comparison indicates that while MXene offers exceptional volumetric capacitance, the overall energy-storage performance is heavily dependent on the specific device architecture, voltage window, and electrode compatibility. Regarding device stability and mechanical durability, MXene-based FSCs exhibit excellent flexibility. For instance, braided MXene-based zinc-ion hybrid FSCs have retained 83.58% of their capacity after 5000 cycles and maintained stable behavior under bending [164]. Nevertheless, conventional carbon materials generally possess superior intrinsic chemical inertness. The long-term stability of MXene in practical wearable environments (involving sweat, washing, and oxygen exposure) remains a challenge, highlighting the necessity of protective encapsulation (such as core-shell structures) [105,169]. Finally, regarding scalability, MXene offers a distinct manufacturing advantage. Unlike CNT and graphene fibers, which often require energy-intensive high-temperature CVD or complex chemical reduction processes, MXene dispersions can be processed at room temperature via scalable wet-spinning or continuous coating [170]. This solution processability makes MXene highly compatible with existing textile manufacturing lines. In summary, leveraging the unique high volumetric performance and scalable processing of MXene, while addressing its stability through structural engineering, is the key to advancing its practical application.

7. Conclusions and Outlook

In this review, we summarize the research progress of MXene-based FSCs in terms of fiber preparation methods, supercapacitor charge storage mechanisms, high-performance optimization strategies and practical wearable applications. With the significant development of MXene fiber preparation technology, due to its lightweight, excellent mechanical properties and outstanding conductivity, MXene-based fibers have become a highly promising electrode material for flexible supercapacitors. However, before achieving large-scale and practical applications, several challenges still need to be overcome. Based on this, the following directions are worthy of particular attention.

First, the use of hazardous chemicals in MXene synthesis poses significant safety and environmental concerns. Traditional MXene synthesis typically relies on hydrofluoric acid (HF) or fluoride-containing etchants to selectively remove the A-layer from MAX phases. Although the LiF/HCl etching strategy avoids direct contact with concentrated HF, HF may still be generated during the reaction, necessitating appropriate safety precautions and proper disposal of fluoride-containing waste [75]. To reduce dependence on HF-based processes, alternative synthesis methods have been explored, including fluoride-free electrochemical etching, alkaline etching, and Lewis acidic molten salt etching [76–78]. These approaches offer potential for tailoring MXene surface termination structures and mitigate some risks associated with conventional etching. However, these methods may involve other corrosive reagents, elevated processing temperatures, complex operational procedures, or challenges in achieving stable product quality and high yields. Therefore, future efforts should focus on developing safer, environmentally friendly, and scalable synthesis strategies while improving process efficiency, reagent recovery rates, and waste management.

Secondly, MXene nanosheets are prone to oxidation during storage and processing, with factors such as environment, temperature, and dispersion concentration affecting their oxidative degradation [68,105]. Oxidation may damage the structure of MXene, reduce conductivity, and impair the electrochemical performance of fiber electrodes. To enhance oxidative stability, storage conditions can be optimized by controlling temperature and oxygen exposure levels, while suitable organic solvents can be explored as alternatives to aqueous media. Additionally, studies have shown that adding antioxidants (e.g., sodium L-ascorbate) can inhibit the oxidation of $Ti_3C_2T_x$ MXene nanosheet dispersions [171]. Surface modification and incorporating MXene into polymer-based or hybrid fiber structures also help protect MXene from oxygen and moisture. However, the design of protective layers and additives should be carefully considered to avoid blocking electrochemically active sites or hindering ion transport. Therefore, future research should balance oxidative stability with conductivity and electrochemical activity, while evaluating the long-term stability of MXene-based flexible supercapacitors under practical working conditions, including humidity, repeated bending, and prolonged charge-discharge cycles.

Thirdly, the internal structure of MXene based fibers remains an important factor limiting their electrochemical performance. In highly densely arranged MXene fibers, including certain core-shell structures, the overlap and stacking of MXene nanosheets can result in lower surface utilization efficiency [37]. In addition, it is difficult to achieve layer by layer controllable assembly of MXene and electroactive nanomaterials during the spinning process, which limits the transfer of interfacial charges and the effective utilization of specific surface area (SSA). To address these issues, emerging spinning technologies such as microfluidic assembly can be employed [152]. These methods can more accurately control the assembly of MXene, customize layered MXene structures, and enhance electron transport, ion migration, and accumulation effects. Further optimizing the orientation, interlayer spacing, and pore structure of the nanosheets can improve the accessibility of electrochemical active sites while maintaining the mechanical integrity of the fiber electrode.

Another challenge is the limited energy available from individual FSC devices. Although MXene-based fibers can achieve high volumetric capacitance, the small dimensions of a single fiber inherently limit its total energy-storage capacity. Overcoming this limitation requires a multi-level strategy involving both electrode and device engineering. At the electrode level, controlling MXene interlayer spacing, constructing porous structures, and combining MXene with suitable pseudocapacitive materials can maximize the utilization of active sites and charge-storage performance. At the device level, asymmetric configurations can extend the stable operating voltage window, while series and parallel connections allow the voltage and total capacitance of FSC modules to be tailored for specific electronic loads [163]. Furthermore, integration with energy-harvesting units and power-management circuits may support longer-term and self-sustained wearable operation. However, improvements in energy density should not compromise mechanical flexibility, cycling stability, or textile compatibility. Therefore, future studies should place greater emphasis on the usable energy and practical operating time of complete devices, rather than relying solely on the normalized specific capacitance of individual electrodes.

Finally, the relatively high manufacturing cost of MXene materials is a practical issue in their large-scale production and commercial applications, especially in the cost sensitive field of wearable electronic devices. The overall production cost is influenced by a variety of factors, including the synthesis of MAX precursor, chemical etching, repeated cleaning and stripping, solvent consumption, waste disposal, and subsequent fiber manufacturing [172]. In addition, additional protective treatments and structural engineering may increase manufacturing complexity. In order to improve economic feasibility, future research should consider using low-cost precursor materials, increasing synthesis yields, recycling processing chemicals, optimizing MXene loading in composite fibers, and achieving continuous and automated spinning processes. However, while reducing manufacturing costs, it is necessary to ensure that conductivity, mechanical flexibility, oxidation stability, and electrochemical performance are not affected. Therefore, a systematic technical and economic evaluation as well as a full lifecycle assessment are needed to determine whether MXene based flexible energy storage devices (FSCs) have sufficient performance advantages to offset their manufacturing costs compared to traditional fiber-based energy storage systems. Although the commercialization of MXene fibers in wearable electronic devices still faces many challenges, their excellent performance makes them a promising candidate material for future flexible energy storage devices. Making progress in safer synthesis methods, enhanced antioxidant properties, rational structural design, and economically efficient large-scale production is crucial for transitioning MXene based FSCs from laboratory demonstrations to practical wearable applications.

Author Contributions

X.Z.: conceptualization, investigation, writing—original draft preparation, writing—reviewing and editing; C.L.: investigation, writing—reviewing and editing; G.W.: conceptualization, supervision, writing—reviewing and editing. All authors have read and agreed to the published version of the manuscript.

Funding

The authors gratefully acknowledge financial support from the National Natural Science Foundation of China (22522814, 22278378), Zhejiang Provincial Natural Science Foundation of China (LDQ24E030001), Science Foundation of Zhejiang Sci-Tech University (22212011-Y).

Conflicts of Interest

The authors declare no conflict of interest.

Use of AI and AI-Assisted Technologies

During the preparation of this work, the authors used DeepSeek and ChatGPT for language polishing and proofreading. The authors subsequently reviewed and edited the manuscript and take full responsibility for its content.

References

1. Zhang, Y.; Zheng, X.T.; Zhang, X.; et al. Hybrid Integration of Wearable Devices for Physiological Monitoring. *Chem. Rev.* **2024**, *124*, 10386–10434. https://doi.org/10.1021/acs.chemrev.3c00471.
2. Brasier, N.; Wang, J.; Gao, W.; et al. Applied body-fluid analysis by wearable devices. *Nature* **2024**, *636*, 57–68. https://doi.org/10.1038/s41586-024-08249-4.
3. Won, D.; Bang, J.; Choi, S.H.; et al. Transparent Electronics for Wearable Electronics Application. *Chem. Rev.* **2023**, *123*, 9982–10078. https://doi.org/10.1021/acs.chemrev.3c00139.
4. Wang, F.; Samartzis, N.; Wang, T.; et al. Synthetic Porous Carbons for High-Energy, High-Power Supercapacitors. *Chem. Rev.* **2026**, *126*, 8517–8598. https://doi.org/10.1021/acs.chemrev.6c00037.
5. Ferrero, G.A.; Åvall, G.; Janßen, K.; et al. Solvent Co-Intercalation Reactions for Batteries and Beyond. *Chem. Rev.* **2025**, *125*, 3401–3439. https://doi.org/10.1021/acs.chemrev.4c00805.
6. Liu, S.; Yang, J.; Chen, P.; et al. Flexible Electrodes for Aqueous Hybrid Supercapacitors: Recent Advances and Future Prospects. *Electrochem. Energy Rev.* **2024**, *7*, 25. https://doi.org/10.1007/s41918-024-00222-z.
7. Ding, Y.; Jiang, J.; Wu, Y.; et al. Porous Conductive Textiles for Wearable Electronics. *Chem. Rev.* **2024**, *124*, 1535–1648. https://doi.org/10.1021/acs.chemrev.3c00507.
8. Hu, X.; Liu, L.; Wang, J. Hydrogels for robust thermal management: Mechanism and applications. *Chem. Soc. Rev.* **2026**, *55*, 3432–3468. https://doi.org/10.1039/d5cs01351h.
9. Chen, Y.; Wei, J.; Duyar, M.S.; et al. Carbon-based catalysts for Fischer–Tropsch synthesis. *Chem. Soc. Rev.* **2021**, *50*, 2337–2366. https://doi.org/10.1039/d0cs00905a.
10. Li, B.; Dai, F.; Xiao, Q.; et al. Activated Carbon from Biomass Transfer for High-Energy Density Lithium-Ion Supercapacitors. *Adv. Energy Mater.* **2016**, *6*, 1600802. https://doi.org/10.1002/aenm.201600802.
11. Wu, C.; Chu, D.; Gao, C.; et al. Cooperative and Ordered Cross-Scale Assembly of Carbon Nanotube Fibers. *Adv. Mater.* **2026**, *38*, e74400. https://doi.org/10.1002/adma.74400.
12. Sandoval, S.; Gonçalves, G.; Pérez Barrio, J.; et al. A Comprehensive Review on Filled Carbon Nanotubes: Synthesis, Properties and Applications. *Chem. Rev.* **2026**, *126*, 2283–2390. https://doi.org/10.1021/acs.chemrev.5c00219.
13. Bi, J.; Du, Z.; Sun, J.; et al. On the Road to the Frontiers of Lithium-Ion Batteries: A Review and Outlook of Graphene Anodes. *Adv. Mater.* **2023**, *35*, 2210734. https://doi.org/10.1002/adma.202210734.
14. Carvalho, A.F.; Kulyk, B.; Fernandes, A.J.S.; et al. A Review on the Applications of Graphene in Mechanical Transduction. *Adv. Mater.* **2022**, *34*, 2101326. https://doi.org/10.1002/adma.202101326.
15. Wang, X.; Xiao, Z.; Han, K.; et al. Advances in Fine Structure Optimizations of Layered Transition-Metal Oxide Cathodes for Potassium-Ion Batteries. *Adv. Energy Mater.* **2023**, *13*, 2202861. https://doi.org/10.1002/aenm.202202861.
16. Peng, Z.; Huang, Y.; Bannov, A.G.; et al. Regulating oxygen vacancies and coordination environment of manganese dioxide for enhanced high-mass-loading energy storage. *Energy Environ. Sci.* **2024**, *17*, 3384–3395. https://doi.org/10.1039/d4ee00949e.
17. Cao, M.; Wu, X.; Qiu, D.; et al. Carboxylated cotton fiber-integrated PPy/PANI composites for high-performance flexible supercapacitor electrodes via TEMPO oxidation. *Ind. Chem. Mater.* **2026**. https://doi.org/10.1039/d5im00294j.
18. Singh, G.; Jadoun, S. Tailoring conducting polymers for advanced electrochemical energy storage. *Prog. Mater. Sci.* **2026**, *161*, 101711. https://doi.org/10.1016/j.pmatsci.2026.101711.
19. Li, J.; Yan, X.; Lian, C.; et al. Boosting Extraordinary Capacitive Performance by Porous Structure Engineering of Binders in Activated Carbon-Based Electrodes. *Adv. Energy Mater.* **2025**, *15*, e04231. https://doi.org/10.1002/aenm.202504231.
20. Wu, D.; Sun, F.; Xie, M.; et al. A review on multi-scale structure engineering of carbon-based electrode materials towards dense energy storage for supercapacitors. *J. Energy Chem.* **2025**, *102*, 768–799. https://doi.org/10.1016/j.jechem.2024.11.023.
21. Ahn, J.; Padmajan Sasikala, S.; Jeong, Y.; et al. High-Energy–Density Fiber Supercapacitors Based on Transition Metal Oxide Nanoribbon Yarns for Comprehensive Wearable Electronics. *Adv. Fiber Mater.* **2024**, *6*, 1927–1941. https://doi.org/10.1007/s42765-024-00462-0.
22. Tatrari, G.; Ahmed, M.; Shah, F.U. Synthesis, thermoelectric and energy storage performance of transition metal oxides composites. *Coord. Chem. Rev.* **2024**, *498*, 215470. https://doi.org/10.1016/j.ccr.2023.215470.
23. VahidMohammadi, A.; Rosen, J.; Gogotsi, Y. The world of two-dimensional carbides and nitrides (MXenes). *Science* **2021**, *372*, eabf1581. https://doi.org/10.1126/science.abf1581.
24. Pang, J.; Mendes, R.G.; Bachmatiuk, A.; et al. Applications of 2D MXenes in energy conversion and storage systems. *Chem. Soc. Rev.* **2019**, *48*, 72–133. https://doi.org/10.1039/c8cs00324f.

25. Zhao, Y.; Zhang, J.; Guo, X.; et al. Engineering strategies and active site identification of MXene-based catalysts for electrochemical conversion reactions. *Chem. Soc. Rev.* **2023**, *52*, 3215–3264. https://doi.org/10.1039/d2cs00698g.
26. Li, X.; Huang, Z.; Shuck, C.E.; et al. MXene chemistry, electrochemistry and energy storage applications. *Nat. Rev. Chem.* **2022**, *6*, 389–404. https://doi.org/10.1038/s41570-022-00384-8.
27. Naguib, M.; Kurtoglu, M.; Presser, V.; et al. Two-Dimensional Nanocrystals Produced by Exfoliation of Ti_3AlC_2. *Adv. Mater.* **2011**, *23*, 4248–4253. https://doi.org/10.1002/adma.201102306.
28. Fan, W.; Wang, Q.; Rong, K.; et al. MXene Enhanced 3D Needled Waste Denim Felt for High-Performance Flexible Supercapacitors. *Nano-Micro Lett.* **2024**, *16*, 36. https://doi.org/10.1007/s40820-023-01226-y.
29. Lukatskaya, M.R.; Kota, S.; Lin, Z.; et al. Ultra-high-rate pseudocapacitive energy storage in two-dimensional transition metal carbides. *Nat. Energy* **2017**, *2*, 17105. https://doi.org/10.1038/nenergy.2017.105.
30. Guo, T.; Zhou, D.; Deng, S.; et al. Rational Design of $Ti_3C_2T_x$ MXene Inks for Conductive, Transparent Films. *ACS Nano* **2023**, *17*, 3737–3749. https://doi.org/10.1021/acsnano.2c11180.
31. Usman, K.A.S.; Zhang, J.; Bi, L.; et al. The Future of MXene Fibers. *Adv. Mater.* **2025**, *37*, 2506437. https://doi.org/10.1002/adma.202506437.
32. Seyedin, S.; Yanza, E.R.S.; Razal, J.M. Knittable energy storing fiber with high volumetric performance made from predominantly MXene nanosheets. *J. Mater. Chem. A* **2017**, *5*, 24076–24082. https://doi.org/10.1039/c7ta08355f.
33. Wang, Z.; Qin, S.; Seyedin, S.; et al. High-Performance Biscrolled MXene/Carbon Nanotube Yarn Supercapacitors. *Small* **2018**, *14*, 1802225. https://doi.org/10.1002/smll.201802225.
34. Wang, Z.; Chen, Y.; Yao, M.; et al. Facile fabrication of flexible rGO/MXene hybrid fiber-like electrode with high volumetric capacitance. *J. Power Sources* **2020**, *448*, 227398. https://doi.org/10.1016/j.jpowsour.2019.227398.
35. Zhang, J.; Seyedin, S.; Qin, S.; et al. Highly Conductive $Ti_3C_2T_x$ MXene Hybrid Fibers for Flexible and Elastic Fiber-Shaped Supercapacitors. *Small* **2019**, *15*, 1804732. https://doi.org/10.1002/smll.201804732.
36. Zhang, J.; Uzun, S.; Seyedin, S.; et al. Additive-Free MXene Liquid Crystals and Fibers. *ACS Cent. Sci.* **2020**, *6*, 254–265. https://doi.org/10.1021/acscentsci.9b01217.
37. Li, S.; Fan, Z.; Wu, G.; et al. Assembly of Nanofluidic MXene Fibers with Enhanced Ionic Transport and Capacitive Charge Storage by Flake Orientation. *ACS Nano* **2021**, *15*, 7821–7832. https://doi.org/10.1021/acsnano.1c02271.
38. Liu, L.X.; Chen, W.; Zhang, H.B.; et al. Super-Tough and Environmentally Stable Aramid. Nanofiber@MXene Coaxial Fibers with Outstanding Electromagnetic Interference Shielding Efficiency. *Nano-Micro Lett.* **2022**, *14*, 111. https://doi.org/10.1007/s40820-022-00853-1.
39. Wang, H.; Wang, Y.; Chang, J.; et al. Nacre-Inspired Strong MXene/Cellulose Fiber with Superior Supercapacitive Performance via Synergizing the Interfacial Bonding and Interlayer Spacing. *Nano Lett.* **2023**, *23*, 5663–5672. https://doi.org/10.1021/acs.nanolett.3c01307.
40. Yin, G.; Wu, J.; Ye, L.; et al. Dynamic Adaptive Wrinkle-Structured Silk Fibroin/MXene Composite Fibers for Switchable Electromagnetic Interference Shielding. *Adv. Funct. Mater.* **2025**, *35*, 2314425. https://doi.org/10.1002/adfm.202314425.
41. Liang, Q.; Liu, K.; Xu, T.; et al. Interfacial Modulation of $Ti_3C_2T_x$ MXene by Cellulose Nanofibrils to Construct Hybrid Fibers with High Volumetric Specific Capacitance. *Small* **2024**, *20*, 2307344. https://doi.org/10.1002/smll.202307344.
42. Li, S.; Wang, Y.; Chu, N.; et al. Janus MXene Fiber Constructed via Flake Orientation Engineering. *Adv. Mater.* **2025**, *37*, e11550. https://doi.org/10.1002/adma.202511550.
43. Wang, R.; Jiang, X.; Ding, T.; et al. Interface-engineered MXene/OCNT fibers for high-performance wearable supercapacitors. *Chem. Eng. J.* **2026**, *537*, 176097. https://doi.org/10.1016/j.cej.2026.176097.
44. Cao, W.; Nie, J.; Cao, Y.; et al. A review of how to improve $Ti_3C_2T_x$ MXene stability. *Chem. Eng. J.* **2024**, *496*, 154097. https://doi.org/10.1016/j.cej.2024.154097.
45. Mendhe, A.C.; Rengasamy, M.; Pradeep, H.; et al. Recent advances and insights into carbon-based materials synergistically enhancing MXene for supercapacitor, battery, solar cell, and electrocatalytic applications. *Coord. Chem. Rev.* **2026**, *550*, 217400. https://doi.org/10.1016/j.ccr.2025.217400.
46. Pi, X.; Qi, K.; Wang, H.; et al. $Ti_3C_2T_x$ MXene fiber with interlayer modification to boost ion transfer and adsorption for high-performance capacitance storage. *J. Energy Storage* **2026**, *141*, 119213. https://doi.org/10.1016/j.est.2025.119213.
47. Paul, T.K.; Khaleque, M.A.; Ali, M.R.; et al. MXenes from MAX phases: Synthesis, hybridization, and advances in supercapacitor applications. *RSC Adv.* **2025**, *15*, 8948–8976. https://doi.org/10.1039/d5ra00271k.
48. Kumar, S.; Choi, S.R.; Zain Mehdi, S.M.; et al. $Ti_3C_2T_x$ MXene: An all-rounder material for next-generation solid-state batteries. *J. Energy Chem.* **2026**, *113*, 61–90. https://doi.org/10.1016/j.jechem.2025.09.026.
49. Lukatskaya, M.R.; Mashtalir, O.; Ren, C.E.; et al. Cation Intercalation and High Volumetric Capacitance of Two-Dimensional Titanium Carbide. *Science* **2013**, *341*, 1502–1505. https://doi.org/10.1126/science.1241488.
50. Hu, C.; Bai, Y.; Wang, W.; et al. Recent development review of $Ti_3C_2T_x$ MXene-based microsupercapacitors: A multi-dimensional analysis spanning from underlying mechanisms to integrated applications. *Mater. Horizons* **2025**, *12*, 5539–5569. https://doi.org/10.1039/d5mh00423c.

51. Shao, Y.; El-Kady, M.F.; Sun, J.; et al. Design and Mechanisms of Asymmetric Supercapacitors. *Chem. Rev.* **2018**, *118*, 9233–9280. https://doi.org/10.1021/acs.chemrev.8b00252.
52. Wang, F.; Wu, X.; Yuan, X.; et al. Latest advances in supercapacitors: From new electrode materials to novel device designs. *Chem. Soc. Rev.* **2017**, *46*, 6816–6854. https://doi.org/10.1039/c7cs00205j.
53. Qian, A.; Hyeon, S.E.; Seo, J.Y.; et al. Capacitance changes associated with cation-transport in free-standing flexible $Ti_3C_2T_x$ (T=O, F, OH) MXene film electrodes. *Electrochim. Acta* **2018**, *266*, 86–93. https://doi.org/10.1016/j.electacta.2018.02.019.
54. Sharma, N.; Godeffroy, L.; Bärmann, P.; et al. Nanoscale chemical imaging of pseudocapacitive charge storage in MXenes. *Energy Environ. Sci.* **2026**, *19*, 680–690. https://doi.org/10.1039/d5ee05809k.
55. Shao, H.; Xu, K.; Wu, Y.C.; et al. Unraveling the Charge Storage Mechanism of $Ti_3C_2T_x$ MXene Electrode in Acidic Electrolyte. *ACS Energy Lett.* **2020**, *5*, 2873–2880. https://doi.org/10.1021/acsenergylett.0c01290.
56. Mu, X.; Wang, D.; Du, F.; et al. Revealing the Pseudo-Intercalation Charge Storage Mechanism of MXenes in Acidic Electrolyte. *Adv. Funct. Mater.* **2019**, *29*, 1902953. https://doi.org/10.1002/adfm.201902953.
57. Zhan, C.; Naguib, M.; Lukatskaya, M.; et al. Understanding the MXene Pseudocapacitance. *J. Phys. Chem. Lett.* **2018**, *9*, 1223–1228. https://doi.org/10.1021/acs.jpclett.8b00200.
58. Lukatskaya, M.R.; Bak, S.M.; Yu, X.; et al. Probing the Mechanism of High Capacitance in 2D Titanium Carbide Using *In Situ* X-Ray Absorption Spectroscopy. *Adv. Energy Mater.* **2015**, *5*, 1500589. https://doi.org/10.1002/aenm.201500589.
59. Zhang, D.; Wang, R.; Wang, X.; et al. *In situ* monitoring redox processes in energy storage using UV–Vis spectroscopy. *Nat. Energy* **2023**, *8*, 567–576. https://doi.org/10.1038/s41560-023-01240-9.
60. Brunet Cabré, M.; Spurling, D.; Martinuz, P.; et al. Isolation of pseudocapacitive surface processes at monolayer MXene flakes reveals delocalized charging mechanism. *Nat. Commun.* **2023**, *14*, 374. https://doi.org/10.1038/s41467-023-35950-1.
61. Neff, T.; Stemmler, F.; Kolb, L.; et al. Revealing the pseudocapacitance charge storage mechanism of sulfur-doped carbon supercapacitors in non-aqueous electrolyte through *in situ* EPR. *J. Mater. Chem. A* **2026**, *14*, 10745–10754. https://doi.org/10.1039/d5ta07697h.
62. Bo, Z.; Wang, R.; Wang, B.; et al. Ion desolvation for boosting the charge storage performance in Ti_3C_2 MXene electrode. *Nat. Commun.* **2025**, *16*, 3813. https://doi.org/10.1038/s41467-025-58700-x.
63. Wang, X.; Mathis, T.S.; Li, K.; et al. Influences from solvents on charge storage in titanium carbide MXenes. *Nat. Energy* **2019**, *4*, 241–248. https://doi.org/10.1038/s41560-019-0339-9.
64. Zhang, T.; Chang, L.; Zhang, X.; et al. Simultaneously tuning interlayer spacing and termination of MXenes by Lewis-basic halides. *Nat. Commun.* **2022**, *13*, 6731. https://doi.org/10.1038/s41467-022-34569-y.
65. Liu, L.; Raymundo-Piñero, E.; Sunny, S.; et al. Role of Surface Terminations for Charge Storage of $Ti_3C_2T_x$ MXene Electrodes in Aqueous Acidic Electrolyte. *Angew. Chem. Int. Ed.* **2024**, *63*, e202319238. https://doi.org/10.1002/anie.202319238.
66. Köps, L.; Kreth, F.A.; Klein, M.; et al. An in-depth investigation into the influence of temperature on the electrochemical behavior of electric double-layer capacitors containing ethyl isopropyl sulfone-based electrolytes. *J. Power Sources* **2023**, *581*, 233480. https://doi.org/10.1016/j.jpowsour.2023.233480.
67. Ji, X.; Liu, C.; Liu, P.; et al. Energetic variational approach for prediction of thermal electrokinetics in charging and discharging processes of electrical double layer capacitors. *J. Power Sources* **2022**, *551*, 232184. https://doi.org/10.1016/j.jpowsour.2022.232184.
68. Doo, S.; Chae, A.; Kim, D.; et al. Mechanism and Kinetics of Oxidation Reaction of Aqueous $Ti_3C_2T_x$ Suspensions at Different pHs and Temperatures. *ACS Appl. Mater. Interfaces* **2021**, *13*, 22855–22865. https://doi.org/10.1021/acsami.1c04663.
69. Habib, T.; Zhao, X.; Shah, S.A.; et al. Oxidation stability of $Ti_3C_2T_x$ MXene nanosheets in solvents and composite films. *npj 2D Mater. Appl.* **2019**, *3*, 8. https://doi.org/10.1038/s41699-019-0089-3.
70. Peng, C.; Wang, N.; Huang, X.; et al. High-Temperature Tolerant Flexible Supercapacitors with Redox-Active Water-in-Salt Hydrogel Electrolytes. *ACS Sustain. Chem. Eng.* **2025**, *13*, 13112–13121. https://doi.org/10.1021/acssuschemeng.5c05460.
71. Liu, Q.; Zhao, A.; He, X.; et al. Full-Temperature All-Solid-State $Ti_3C_2T_x$/Aramid Fiber Supercapacitor with Optimal Balance of Capacitive Performance and Flexibility. *Adv. Funct. Mater.* **2021**, *31*, 2010944. https://doi.org/10.1002/adfm.202010944.
72. Wang, Y.; Guo, T.; Tian, Z.; et al. MXenes for Energy Harvesting. *Adv. Mater.* **2022**, *34*, 2108560. https://doi.org/10.1002/adma.202108560.
73. Zhang, Y.Z.; El-Demellawi, J.K.; Jiang, Q.; et al. MXene hydrogels: Fundamentals and applications. *Chem. Soc. Rev.* **2020**, *49*, 7229–7251. https://doi.org/10.1039/d0cs00022a.
74. Anasori, B.; Lukatskaya, M.R.; Gogotsi, Y. 2D metal carbides and nitrides (MXenes) for energy storage. *Nat. Rev. Mater.* **2017**, *2*, 16098. https://doi.org/10.1038/natrevmats.2016.98.
75. Ghidiu, M.; Lukatskaya, M.R.; Zhao, M.Q.; et al. Conductive two-dimensional titanium carbide 'clay' with high volumetric capacitance. *Nature* **2014**, *516*, 78–81. https://doi.org/10.1038/nature13970.
76. Sun, W.; Shah, S.A.; Chen, Y.; et al. Electrochemical etching of Ti_2AlC to Ti_2CT_x (MXene) in low-concentration hydrochloric acid solution. *J. Mater. Chem. A* **2017**, *5*, 21663–21668. https://doi.org/10.1039/c7ta05574a.

77. Li, T.; Yao, L.; Liu, Q.; et al. Fluorine-Free Synthesis of High-Purity $Ti_3C_2T_x$ (T=OH, O) via Alkali Treatment. *Angew. Chem. Int. Ed.* **2018**, *57*, 6115–6119. https://doi.org/10.1002/anie.201800887.
78. Li, M.; Lu, J.; Luo, K.; et al. Element Replacement Approach by Reaction with Lewis Acidic Molten Salts to Synthesize Nanolaminated MAX Phases and MXenes. *J. Am. Chem. Soc.* **2019**, *141*, 4730–4737. https://doi.org/10.1021/jacs.9b00574.
79. Shi, H.; Zhang, P.; Liu, Z.; et al. Ambient-Stable Two-Dimensional Titanium Carbide (MXene) Enabled by Iodine Etching. *Angew. Chem. Int. Ed.* **2021**, *60*, 8689–8693. https://doi.org/10.1002/anie.202015627.
80. Zhu, K.; Jin, Y.; Du, F.; et al. Synthesis of Ti_2CT MXene as electrode materials for symmetric supercapacitor with capable volumetric capacitance. *J. Energy Chem.* **2019**, *31*, 11–18. https://doi.org/10.1016/j.jechem.2018.03.010.
81. VahidMohammadi, A.; Hadjikhani, A.; Shahbazmohamadi, S.; et al. Two-Dimensional Vanadium Carbide (MXene) as a High-Capacity Cathode Material for Rechargeable Aluminum Batteries. *ACS Nano* **2017**, *11*, 11135–11144. https://doi.org/10.1021/acsnano.7b05350.
82. Naguib, M.; Halim, J.; Lu, J.; et al. New Two-Dimensional Niobium and Vanadium Carbides as Promising Materials for Li-Ion Batteries. *J. Am. Chem. Soc.* **2013**, *135*, 15966–15969. https://doi.org/10.1021/ja405735d.
83. Naguib, M.; Mashtalir, O.; Carle, J.; et al. Two-Dimensional Transition Metal Carbides. *ACS Nano* **2012**, *6*, 1322–1331. https://doi.org/10.1021/nn204153h.
84. Tao, Q.; Dahlqvist, M.; Lu, J.; et al. Two-dimensional $Mo_{1.33}C$ MXene with divacancy ordering prepared from parent 3D laminate with in-plane chemical ordering. *Nat. Commun.* **2017**, *8*, 14949. https://doi.org/10.1038/ncomms14949.
85. Zhou, J.; Dahlqvist, M.; Björk, J.; et al. Atomic Scale Design of MXenes and Their Parent Materials—From Theoretical and Experimental Perspectives. *Chem. Rev.* **2023**, *123*, 13291–13322. https://doi.org/10.1021/acs.chemrev.3c00241.
86. Alhabeb, M.; Maleski, K.; Anasori, B.; et al. Guidelines for Synthesis and Processing of Two-Dimensional Titanium Carbide ($Ti_3C_2T_x$ MXene). *Chem. Mater.* **2017**, *29*, 7633–7644. https://doi.org/10.1021/acs.chemmater.7b02847.
87. Liu, F.; Zhou, A.; Chen, J.; et al. Preparation of Ti_3C_2 and Ti_2C MXenes by fluoride salts etching and methane adsorptive properties. *Appl. Surf. Sci.* **2017**, *416*, 781–789. https://doi.org/10.1016/j.apsusc.2017.04.239.
88. Venkateshalu, S.; Shariq, M.; Kim, B.; et al. Recent advances in MXenes: Beyond Ti-only systems. *J. Mater. Chem. A* **2023**, *11*, 13107–13132. https://doi.org/10.1039/d3ta01590d.
89. Nouseen, S.; Pumera, M. Electrochemical etching of MXenes: Mechanism, challenges and future outlooks. *J. Mater. Chem. A* **2025**, *13*, 34055–34084. https://doi.org/10.1039/d5ta04176g.
90. Chen, J.; Chen, M.; Zhou, W.; et al. Simplified Synthesis of Fluoride-Free $Ti_3C_2T_x$ via Electrochemical Etching toward High-Performance Electrochemical Capacitors. *ACS Nano* **2022**, *16*, 2461–2470. https://doi.org/10.1021/acsnano.1c09004.
91. Yang, S.; Zhang, P.; Wang, F.; et al. Fluoride-Free Synthesis of Two-Dimensional Titanium Carbide (MXene) Using A Binary Aqueous System. *Angew. Chem. Int. Ed.* **2018**, *57*, 15491–15495. https://doi.org/10.1002/anie.201809662.
92. Khan, U.; Gao, B.; Kong, L.B.; et al. Green synthesis of fluorine-free MXene via hydrothermal process: A sustainable approach for proton supercapacitor electrodes. *Electrochim. Acta* **2024**, *475*, 143651. https://doi.org/10.1016/j.electacta.2023.143651.
93. Kulkarni, M.; Lalic, A.; Balu, R.; et al. Hydrothermal synthesis of MXenes in alkali environment and development of MXene/PEDOT:PSS composite electrodes for supercapacitor applications. *MRS Adv.* **2024**, *9*, 1310–1317. https://doi.org/10.1557/s43580-024-00951-9.
94. Li, Y.; Shao, H.; Lin, Z.; et al. A general Lewis acidic etching route for preparing MXenes with enhanced electrochemical performance in non-aqueous electrolyte. *Nat. Mater.* **2020**, *19*, 894–899. https://doi.org/10.1038/s41563-020-0657-0. Correction in *Nat. Mater.* **2021**, *20*, 571.
95. Iakunkov, A.; Boulanger, N.; Gurzeda, B.; et al. *In Situ* X-ray Diffraction Study of MXene Synthesis by the Reaction of Ti_3AlC_2 with Molten Zinc and Tin Chlorides. *Chem. Mater.* **2025**, *37*, 1132–1142. https://doi.org/10.1021/acs.chemmater.4c02989.
96. Jawaid, A.; Hassan, A.; Neher, G.; et al. Halogen Etch of Ti_3AlC_2 MAX Phase for MXene Fabrication. *ACS Nano* **2021**, *15*, 2771–2777. https://doi.org/10.1021/acsnano.0c08630.
97. Zhu, J.; Zhu, S.; Cui, Z.; et al. Solvent-free one-step green synthesis of MXenes by "gas-phase selective etching". *Energy Storage Mater.* **2024**, *70*, 103503. https://doi.org/10.1016/j.ensm.2024.103503.
98. Li, D.; Zheng, W.; Ghorbani-Asl, M.; et al. Triphasic synthesis of MXenes with uniform and controlled halogen terminations. *Nat. Synth.* **2026**, *5*, 516–526. https://doi.org/10.1038/s44160-025-00970-w.
99. Ye, F.; Xu, B.; Chen, R.; et al. The Influence of Nano- and Micron-size of MXene Flakes on the Electrochemical Performance. *Electron. Mater. Lett.* **2023**, *19*, 527–533. https://doi.org/10.1007/s13391-023-00418-3.
100. Zhang, Y.; Pi, X.; Xu, J.; et al. Assembly of flexible $Ti_3C_2T_x$ fiber with promoted ionic transport by constructing hierarchical flakes size for high-performance fiber shaped supercapacitors. *J. Alloys Compd.* **2025**, *1014*, 178613. https://doi.org/10.1016/j.jallcom.2025.178613.
101. Sikdar, A.; Héraly, F.; Zhang, H.; et al. Hierarchically Porous 3D Freestanding Holey-MXene Framework via Mild Oxidation of Self-Assembled MXene Hydrogel for Ultrafast Pseudocapacitive Energy Storage. *ACS Nano* **2024**, *18*, 3707–3719. https://doi.org/10.1021/acsnano.3c11551.

102. Liu, H.; Liu, Y.; Xu, D.; et al. 3D Cross-linked $Ti_3C_2T_x$-Ca-SA films with expanded $Ti_3C_2T_x$ interlayer spacing as freestanding electrode for all-solid-state flexible pseudocapacitor. *J. Colloid Interface Sci.* **2022**, *610*, 295–303. https://doi.org/10.1016/j.jcis.2021.10.127.
103. Hope, M.A.; Forse, A.C.; Griffith, K.J.; et al. NMR reveals the surface functionalisation of Ti_3C_2 MXene. *Phys. Chem. Chem. Phys.* **2016**, *18*, 5099–5102. https://doi.org/10.1039/c6cp00330c.
104. Natu, V.; Sokol, M.; Verger, L.; et al. Effect of Edge Charges on Stability and Aggregation of $Ti_3C_2T_z$ MXene Colloidal Suspensions. *J. Phys. Chem. C* **2018**, *122*, 27745–27753. https://doi.org/10.1021/acs.jpcc.8b08860.
105. Zhang, C.J.; Pinilla, S.; McEvoy, N.; et al. Oxidation Stability of Colloidal Two-Dimensional Titanium Carbides (MXenes). *Chem. Mater.* **2017**, *29*, 4848–4856. https://doi.org/10.1021/acs.chemmater.7b00745.
106. Maleski, K.; Mochalin, V.N.; Gogotsi, Y. Dispersions of Two-Dimensional Titanium Carbide MXene in Organic Solvents. *Chem. Mater.* **2017**, *29*, 1632–1640. https://doi.org/10.1021/acs.chemmater.6b04830.
107. Tan, J.; Fan, B.; Zhang, P.; et al. Ultralong Stability of $Ti_3C_2T_x$-MXene Dispersion through Synergistic Regulation of Storage Environment and Defect Capping with Tris-HCl Buffering. *Small Methods* **2024**, *8*, 2301689. https://doi.org/10.1002/smtd.202301689.
108. Akuzum, B.; Maleski, K.; Anasori, B.; et al. Rheological Characteristics of 2D Titanium Carbide (MXene) Dispersions: A Guide for Processing MXenes. *ACS Nano* **2018**, *12*, 2685–2694. https://doi.org/10.1021/acsnano.7b08889.
109. Kim, J.G.; Yun, T.; Choi, G.B.; et al. Surface Tension-Driven Self-Planarization of MXene Liquid Crystalline Fiber for High-Performance Energy Storage. *ACS Nano* **2025**, *19*, 16053–16063. https://doi.org/10.1021/acsnano.5c03111.
110. Zhou, Y.; Yin, L.; Xiang, S.; et al. Unleashing the Potential of MXene-Based Flexible Materials for High-Performance Energy Storage Devices. *Adv. Sci.* **2024**, *11*, 2304874. https://doi.org/10.1002/advs.202304874.
111. Repon, M.R.; Mikučionienė, D.; Paul, T.K.; et al. Architectural design and affecting factors of MXene-based textronics for real-world application. *RSC Adv.* **2024**, *14*, 16093–16116. https://doi.org/10.1039/d4ra01820f.
112. Rupanty, N.S.; Ghosh, J.; Noor, T.; et al. Advances in Wearable Technology: MXene-Based Multifunctional and Biomedical Smart Textiles. *ACS Omega* **2026**, *11*, 197–228. https://doi.org/10.1021/acsomega.5c08488.
113. Inman, A.; Hryhorchuk, T.; Bi, L.; et al. Wearable energy storage with MXene textile supercapacitors for real world use. *J. Mater. Chem. A* **2023**, *11*, 3514–3523. https://doi.org/10.1039/d2ta08995e.
114. Uzun, S.; Seyedin, S.; Stoltzfus, A.L.; et al. Knittable and Washable Multifunctional MXene-Coated Cellulose Yarns. *Adv. Funct. Mater.* **2019**, *29*, 1905015. https://doi.org/10.1002/adfm.201905015.
115. Levitt, A.; Hegh, D.; Phillips, P.; et al. 3D knitted energy storage textiles using MXene-coated yarns. *Mater. Today* **2020**, *34*, 17–29. https://doi.org/10.1016/j.mattod.2020.02.005.
116. Zhang, H.; Ji, H.; Chen, J.; et al. A multi-scale MXene coating method for preparing washable conductive cotton yarn and fabric. *Ind. Crops Prod.* **2022**, *188*, 115653. https://doi.org/10.1016/j.indcrop.2022.115653.
117. Duygun, İ.K.; Küçükelyas, B.; Bedeloğlu, A. Structurally integrated $Ti_3C_2T_x$ MXene/cotton fabric electrodes for supercapacitor applications. *Mater. Res. Bull.* **2024**, *180*, 113042. https://doi.org/10.1016/j.materresbull.2024.113042.
118. Jorn-am, T.; Kim, C.H.; Chanthad, C.; et al. Scalable Interfacial Design of CNT/MXene Hybrid Yarns for Durable and Flexible Supercapacitors. *Small* **2025**, *21*, e08739. https://doi.org/10.1002/smll.202508739.
119. Pathak, I.; Acharya, D.; Chhetri, K.; et al. $Ti_3C_2T_x$ MXene embedded metal–organic framework-based porous electrospun carbon nanofibers as a freestanding electrode for supercapacitors. *J. Mater. Chem. A* **2023**, *11*, 5001–5014. https://doi.org/10.1039/d2ta09726e.
120. Wei, Y.M.; Kumar, K.D.; Zhang, L.; et al. Pseudocapacitive materials for energy storage: Properties, mechanisms, and applications in supercapacitors and batteries. *Front. Chem.* **2025**, *13*, 1636683. https://doi.org/10.3389/fchem.2025.1636683.
121. Han, Y.; Ge, Y.; Chao, Y.; et al. Recent progress in 2D materials for flexible supercapacitors. *J. Energy Chem.* **2018**, *27*, 57–72. https://doi.org/10.1016/j.jechem.2017.10.033.
122. Wu, W.; Li, X.; Liu, Y.; et al. Electrospun MXene-based nanofibrous membranes: Multifunctional integration, challenges, and emerging applications. *Prog. Org. Coat.* **2025**, *208*, 109480. https://doi.org/10.1016/j.porgcoat.2025.109480.
123. Levitt, A.S.; Alhabeb, M.; Hatter, C.B.; et al. Electrospun MXene/carbon nanofibers as supercapacitor electrodes. *J. Mater. Chem. A* **2019**, *7*, 269–277. https://doi.org/10.1039/c8ta09810g.
124. Mokhtari, F.; Groetsch, T.; Heidarian, P.; et al. Functionalizing PAN Carbon Nanofibers Using $Ti_3C_2T_x$ MXene for Improved Thermal and Electrochemical Behavior. *Macromol. Rapid Commun.* **2025**, *46*, e00429. https://doi.org/10.1002/marc.202500429.
125. Zhang, H.; Tang, H.; Fang, L.; et al. A high charging rate self-charging power system with Zeolitic Imidazolate Framework (ZIF-8)@MXene/carbon nanofibers based micro-supercapacitors for wearable electronics. *Chem. Eng. J.* **2025**, *522*, 167535. https://doi.org/10.1016/j.cej.2025.167535.
126. Lima, M.D.; Fang, S.; Lepró, X.; et al. Biscrolling Nanotube Sheets and Functional Guests into Yarns. *Science* **2011**, *331*, 51–55. https://doi.org/10.1126/science.1195912.

127. Park, J.W.; Lee, D.Y.; Kim, H.; et al. Highly loaded MXene/carbon nanotube yarn electrodes for improved asymmetric supercapacitor performance. *MRS Commun.* **2019**, *9*, 114–121. https://doi.org/10.1557/mrc.2019.7.
128. Gao, X.; Du, X.; Mathis, T.S.; et al. Maximizing ion accessibility in MXene-knotted carbon nanotube composite electrodes for high-rate electrochemical energy storage. *Nat. Commun.* **2020**, *11*, 6160. https://doi.org/10.1038/s41467-020-19992-3.
129. Hou, K.; Shi, X.; Yuan, J.; et al. Stretchable PU@CNT/MXene Fiber Fabricated by External Tension for High Performance Strain Sensor and Supercapacitor. *Adv. Mater. Technol.* **2023**, *8*, 2300479. https://doi.org/10.1002/admt.202300479.
130. Zhang, J.; Lynch, P.A.; Usman, K.A.S.; et al. Mapping MXene Alignment under Shear: An *In Situ* SAXS Study of Size-Dependent Orientation Dynamics. *ACS Nano* **2026**, *20*, 7333–7342. https://doi.org/10.1021/acsnano.5c22370.
131. Yang, Z.; Yang, Y.; Huang, Y.; et al. Wet-spinning of carbon nanotube fibers: Dispersion, processing and properties. *Natl. Sci. Rev.* **2024**, *11*, nwae203. https://doi.org/10.1093/nsr/nwae203.
132. Zhai, H.; Liu, J.; Liu, Z.; et al. Functional Graphene Fiber Materials for Advanced Wearable Applications. *Adv. Fiber Mater.* **2025**, *7*, 443–468. https://doi.org/10.1007/s42765-025-00512-1.
133. Wei, L.; Wang, S.; Shan, M.; et al. Conductive fibers for biomedical applications. *Bioact. Mater.* **2023**, *22*, 343–364. https://doi.org/10.1016/j.bioactmat.2022.10.014.
134. Usman, K.A.S.; Zhang, J.; Marquez, K.P.; et al. Recent advances and opportunities in MXene-based liquid crystals. *InfoMat* **2024**, *6*, e12516. https://doi.org/10.1002/inf2.12516.
135. Woods, M.B.; Beidaghi, M.; Davis, V.A. Phase Behavior and Rheological Properties of Size-Fractionated MXene ($Ti_3C_2T_x$) Dispersions. *Langmuir* **2024**, *40*, 2907–2917. https://doi.org/10.1021/acs.langmuir.3c02851.
136. Eom, W.; Shin, H.; Ambade, R.B.; et al. Large-scale wet-spinning of highly electroconductive MXene fibers. *Nat. Commun.* **2020**, *11*, 2825. https://doi.org/10.1038/s41467-020-16671-1.
137. Shin, H.; Eom, W.; Lee, K.H.; et al. Highly Electroconductive and Mechanically Strong $Ti_3C_2T_x$ MXene Fibers Using a Deformable MXene Gel. *ACS Nano* **2021**, *15*, 3320–3329. https://doi.org/10.1021/acsnano.0c10255.
138. Huang, C.; Chen, Y.; Zhang, T.; et al. Continuous MXene fibers with near-gigapascal tensile strength via radial confinement and axial stretching. *Nat. Commun.* **2026**, *17*, 1277. https://doi.org/10.1038/s41467-025-68038-z.
139. Cao, H.; Neal, N.N.; Pas, S.; et al. Architecting MXenes in polymer composites. *Prog. Polym. Sci.* **2024**, *153*, 101830. https://doi.org/10.1016/j.progpolymsci.2024.101830.
140. Khumujam, D.D.; Kshetri, T.; Singh, T.I.; et al. Fibrous asymmetric supercapacitor based on wet spun MXene/PAN Fiber-derived multichannel porous MXene/CF negatrode and $NiCo_2S_4$ electrodeposited MXene/CF positrode. *Chem. Eng. J.* **2022**, *449*, 137732. https://doi.org/10.1016/j.cej.2022.137732.
141. Alipoori, S.; Mohamadi, A.; Taheri, S.M.R.; et al. Next-generation wearable electronics: The role of flexible fiber-based supercapacitors. *J. Energy Storage* **2026**, *167*, 122484. https://doi.org/10.1016/j.est.2026.122484.
142. Cheng, W.; Sun, L.; Dong, J.; et al. Application progress and challenges of 1D fiber electrodes in wearable devices. *Energy Storage Mater.* **2025**, *75*, 104059. https://doi.org/10.1016/j.ensm.2025.104059.
143. He, N.; Patil, S.; Qu, J.; et al. Effects of Electrolyte Mediation and MXene Size in Fiber-Shaped Supercapacitors. *ACS Appl. Energy Mater.* **2020**, *3*, 2949–2958. https://doi.org/10.1021/acsaem.0c00024.
144. Kalliguddi, S.; Bhajantri, R.F.; Chalawadi, S.; et al. Influence of Sodium Tungstate on Dielectric and Electrochemical Properties ofPVA/NACMCPolymer Nanocomposites for Energy Storage Applications. *J. Appl. Polym. Sci.* **2026**, *143*, e57971. https://doi.org/10.1002/app.57971.
145. Huang, B.; Wang, H.; Liang, S.; et al. Two-dimensional porous cobalt–nickel tungstate thin sheets for high performance supercapattery. *Energy Storage Mater.* **2020**, *32*, 105–114. https://doi.org/10.1016/j.ensm.2020.07.014.
146. Patil, D.J.; Malavekar, D.B.; Kim, J.H.; et al. Facial synthesis of reduced graphene oxide—Amorphous nickel tungstate composite for flexible hybrid asymmetric solid state supercapacitor application. *J. Energy Storage* **2023**, *72*, 108729. https://doi.org/10.1016/j.est.2023.108729.
147. Wang, Y.; Zheng, Y.; Zhao, J.; et al. Assembling free-standing and aligned tungstate/MXene fiber for flexible lithium and sodium-ion batteries with efficient pseudocapacitive energy storage. *Energy Storage Mater.* **2020**, *33*, 82–87. https://doi.org/10.1016/j.ensm.2020.06.018.
148. Yang, F.; Zhao, X.; Usman, K.A.S.; et al. Engineering coaxial MXene@CNT fibers via wet-spinning for balanced mechanical, electrical, and electrochemical performance. *J. Energy Storage* **2025**, *137*, 118719. https://doi.org/10.1016/j.est.2025.118719.
149. Shi, F.; Dai, H.; He, N.; et al. Coaxial spinning of $Ti_3C_2T_x$ MXene fibers with spontaneous radial densification achieves simultaneous improvements in both mechanical strength and charge storage ability. *Nanoscale* **2026**, *18*, 4800–4809. https://doi.org/10.1039/d5nr04025f.
150. Han, K.; Lee, E.; Yun, J.; et al. Stretchable conductive Fibers: A quantitative and strategic review from materials to applications. *J. Mater. Res. Technol.* **2026**, *40*, 1769–1793. https://doi.org/10.1016/j.jmrt.2025.12.232.

151. Seyedin, S.; Uzun, S.; Levitt, A.; et al. MXene Composite and Coaxial Fibers with High Stretchability and Conductivity for Wearable Strain Sensing Textiles. *Adv. Funct. Mater.* **2020**, *30*, 1910504. https://doi.org/10.1002/adfm.201910504.
152. Wu, G.; Sun, S.; Zhu, X.; et al. Microfluidic Fabrication of Hierarchical-Ordered ZIF-L(Zn)@$Ti_3C_2T_x$ Core–Sheath Fibers for High-Performance Asymmetric Supercapacitors. *Angew. Chem. Int. Ed.* **2022**, *61*, e202115559. https://doi.org/10.1002/anie.202115559.
153. Levitt, A.; Seyedin, S.; Zhang, J.; et al. Bath Electrospinning of Continuous and Scalable Multifunctional MXene-Infiltrated Nanoyarns. *Small* **2020**, *16*, 2002158. https://doi.org/10.1002/smll.202002158.
154. Liu, L.X.; Chen, W.; Zhang, H.B.; et al. Tough and electrically conductive $Ti_3C_2T_x$ MXene–based core–shell fibers for high–performance electromagnetic interference shielding and heating application. *Chem. Eng. J.* **2022**, *430*, 133074. https://doi.org/10.1016/j.cej.2021.133074.
155. Zhao, X.; Zhang, J.; Lv, K.; et al. Carbon nanotubes boosts the toughness and conductivity of wet-spun MXene fibers for fiber-shaped super capacitors. *Carbon* **2022**, *200*, 38–46. https://doi.org/10.1016/j.carbon.2022.08.045.
156. Gu, J.; Li, F.; Zhu, Y.; et al. Extremely Robust and Multifunctional Nanocomposite Fibers for Strain-Unperturbed Textile Electronics. *Adv. Mater.* **2023**, *35*, 2209527. https://doi.org/10.1002/adma.202209527.
157. Usman, K.A.S.; Yao, Y.; Bacal, C.J.O.; et al. Robust biocompatible fibers from silk fibroin coated MXene sheets. *Adv. Mater. Technol.* **2023**, *10*, 2201634.
158. Dai, H.; Chang, J.; Yang, J.; et al. Bio-Inspired Interfacial Engineering of MXene Fibers Toward Synergistic Improvement in Mechanical Strength and Electrochemical Performance. *Adv. Funct. Mater.* **2024**, *34*, 2312654. https://doi.org/10.1002/adfm.202312654.
159. Zhao, G.; Sui, C.; Miao, L.; et al. Strong and continuous MXene/sodium alginate composite fibers prepared by immersion rotary jet spinning process with outstanding electromagnetic interference shielding performance. *Chem. Eng. J.* **2023**, *469*, 143983. https://doi.org/10.1016/j.cej.2023.143983.
160. Wang, H.; Zhao, W.; Zhang, Z.; et al. Synergizing Electron and Ion Transports of $Ti_3C_2T_x$ MXene Fiber via Dot-Sheet Heterostructure and Covalent Ti–C–Ti Cross-Linking for Efficient Charge Storage and Thermal Management. *Adv. Funct. Mater.* **2024**, *34*, 2408508. https://doi.org/10.1002/adfm.202408508.
161. Ananna, J.S.; Rahman, M.T.U.; Saha, P.; et al. Supercapacitors beyond energy storage: Multi-functional devices for sensing, actuation, and smart systems. *Sustain. Mater. Technol.* **2026**, *47*, e01840. https://doi.org/10.1016/j.susmat.2025.e01840.
162. Fang, X.; Falak, U.; Rasheed, A.; et al. Recent Advances in Fiber-Shaped Supercapacitors for Flexible and Wearable Energy-Storage Applications. *Chem. Mater.* **2026**, *38*, 586–606. https://doi.org/10.1021/acs.chemmater.5c02828.
163. Jiang, Q.; Kurra, N.; Alhabeb, M.; et al. All Pseudocapacitive MXene-RuO_2 Asymmetric Supercapacitors. *Adv. Energy Mater.* **2018**, *8*, 1703043. https://doi.org/10.1002/aenm.201703043.
164. Shi, B.; Li, L.; Chen, A.; et al. Continuous Fabrication of $Ti_3C_2T_x$ MXene-Based Braided Coaxial Zinc-Ion Hybrid Supercapacitors with Improved Performance. *Nano-Micro Lett.* **2022**, *14*, 34. https://doi.org/10.1007/s40820-021-00757-6.
165. Sharma, S.; Shukla, S.K.; Singh, A.; et al. E-Textiles in Biomedicine: Real Time Sensing, Energy Storage, and Therapeutic Applications. *Adv. Mater. Interfaces* **2026**, *13*, e00672. https://doi.org/10.1002/admi.202500672.
166. He, Y.; Su, J.; Guo, C.; et al. Wet-Spun Core–Sheath Fibers for Smart Wearables. *Adv. Mater. Technol.* **2025**, *10*, e00921. https://doi.org/10.1002/admt.202500921.
167. Chu, M.; Xie, F.; Cao, J.; et al. Flexible zinc-ion hybrid supercapacitors with high energy density and long cycling life enabled by the microfluidic assembly of MXene composite fibers. *J. Mater. Chem. A* **2026**, *14*, 23281–23293. https://doi.org/10.1039/d6ta02290a.
168. Li, D.; Gu, J.; Zhang, X.; et al. Highly Flexible Fiber Supercapacitors with Ultra-High Energy Density for Energy Storage Electronic Textiles. *Nano Lett.* **2026**, *26*, 2484–2492. https://doi.org/10.1021/acs.nanolett.5c05637.
169. Jug, L.; Hribernik, S.; Ojstršek, A. Synergic effect of large MXene nanosheets and protective coatings on improved electroconductivity and wash durability of MXene/polymer-modified cotton fabric. *Prog. Org. Coatings* **2025**, *200*, 109062. https://doi.org/10.1016/j.porgcoat.2025.109062.
170. Bi, L.; Perry, W.; Wang, R.J.; et al. MXene Functionalized Kevlar Yarn via Automated, Continuous Dip Coating. *Adv. Funct. Mater.* **2024**, *34*, 2312434. https://doi.org/10.1002/adfm.202312434.
171. Zhao, X.; Vashisth, A.; Prehn, E.; et al. Antioxidants Unlock Shelf-Stable $Ti_3C_2T_x$ (MXene) Nanosheet Dispersions. *Matter* **2019**, *1*, 513–526. https://doi.org/10.1016/j.matt.2019.05.020.
172. Zaed, M.A.; Tan, K.H.; Abdullah, N.; et al. Cost analysis of MXene for low-cost production, and pinpointing of its economic footprint. *Open Ceram.* **2024**, *17*, 100526. https://doi.org/10.1016/j.oceram.2023.100526.